Available online at www.sciencedirect.com

ScienceDirect

Geochimica et Cosmochimica Acta 325 (2022) 1–24

Geochimica et Cosmochimica Acta

www.elsevier.com/locate/gca

In-situ O-isotope analysis of relict spinel and forsterite in small (<200 μm) Antarctic micrometeorites – Samples of chondrules & CAIs from carbonaceous chondrites

N.G. Rudraswami [a,*], M.D. Suttle [b], Y. Marrocchi [c], S. Taylor [d], J. Villeneuve [c]

[a] National Institute of Oceanography (Council of Scientific and Industrial Research), Dona Paula, Goa 403004, India
[b] School of Physical Sciences, The Open University, Walton Hall, Milton Keynes MK7 6AA, UK
[c] CRPG, CNRS, Université de Lorraine, UMR 7358, Vandoeuvre-les-Nancy F-54501, France
[d] Cold Regions Research and Engineering Laboratory, 72 Lyme Road, Hanover, NH 03755-1290, USA

Received 25 April 2021; accepted in revised form 11 March 2022; available online 19 March 2022

Abstract

We report high-precision secondary ion mass spectrometer triple oxygen isotope systematics (95 individual analyses) from 37 micrometeorites (MMs) collected from South Pole Water Well (SPWW), Antarctica. The study population focuses on unmelted coarse-grained (Cg) MMs ($n = 23$) with both multiple ($n = 14$) and single-mineral ($n = 9$) varieties investigated. We also analysed relict minerals in porphyritic cosmic spherules ($n = 13$) and the relict matrix in a single scoriaceous fine-grained (Fg) MM. The target minerals investigated are primarily olivine (Fo ~ 43–99%) and spinel. Textural, chemical and isotopic data confirm that both olivine and spinel grains have retained their pre-atmospheric O-isotope compositions, allowing inferences to be drawn about their formation and parent body affinities. We separate the study population into three groups: spinel-free particles (consisting of the CgMMs and PO cosmic spherules), spinel-bearing MMs and the single FgMM.

Olivine grains in spinel-free MMs vary between $\delta^{17}O$: −12.6‰ and +3.5‰, $\delta^{18}O$: −9.6‰ and +7.5‰, and $\Delta^{17}O$: −9.5‰ and +1.3‰ and define a slope-1 profile in $\delta^{18}O$–$\delta^{17}O$ isotope space. They are most likely fragmented chondrules, with both type I and type II varieties represented. Their observed Mg#-$\Delta^{17}O$ distribution is best explained by a mixture of CM chondrules and either CR chondrules, Tagish Lake chondrules or WILD2 cometary silicates. One of these chondrule-like MMs has an isotopically heterogeneous composition, characterised by a single olivine grain with a markedly ^{16}O-rich composition ($\Delta^{17}O$: −16.3‰), suggesting it is a relict silicate fragment of AOA material that was incorporated into the chondrule precursor.

We analysed 11 spinel grains in five spinel-bearing MMs. In all instances spinels are nearly pure $MgAl_2O_4$ with isotopically light (^{16}O-rich) compositions (ranging from $\delta^{17}O$: −34.4‰ to −0.9‰, $\delta^{18}O$: −30.8‰ to +11.0‰, and $\Delta^{17}O$: −18.3‰ to −4.4‰). They are therefore ^{16}O-poor relative to spinel found in unaltered CAIs, indicating a different origin. Grains with high Cr_2O_3 contents (>0.5 wt.%) are interpreted originating from Al-rich chondrule precursors, while low Cr_2O_3 spinels (<0.5 wt.%) are interpreted as CAI-derived material affected by parent body aqueous alteration.

Finally, we report a single FgMM with a ^{16}O-poor composition ($\Delta^{17}O > 0$‰ and $\delta^{18}O > +15.0$‰). This particle adds to our growing inventory of water-rich C-type asteroid samples united by their formation history which is characterised by accretion of abundant heavy water.

Our work strongly supports findings from earlier in-situ O-isotope studies, concluding that small MMs overwhelmingly sample material from CC parent bodies and that CgMMs largely sample chondrules and, to a lesser extent, CAI material.

* Corresponding author.
E-mail addresses: rudra@nio.org, rudraswami@gmail.com (N.G. Rudraswami).

https://doi.org/10.1016/j.gca.2022.03.015

The analysis of CgMMs therefore provides insights into the primitive O-isotope reservoirs that were present in the early solar system and how they interacted.

Keywords: Micrometeorites; Oxygen isotope; Chondrules; Spinel; Antarctic

1. INTRODUCTION

Micrometeorites (MMs) are among the smallest size fractions of extraterrestrial material (~50–2000 μm, Taylor et al., 1998; Genge et al., 2008; Folco and Cordier, 2015). They are released from their parent bodies as dust and spiral inwards towards the Sun over geologically rapid timescales (<100 ka, Wyatt and Whipple, 1950; Gonczi et al., 1982). A small fraction of the inner solar system's dust complex intersects Earth's orbit and is captured by its gravity (Nesvorný et al., 2006). Infalling cosmic dust grains are subject to flash heating during atmospheric entry which results in the complete vaporisation of most particles (Love and Brownlee, 1991). Those that do survive entry can be recovered from the Earth's surface as MMs. They sample both asteroids and comets (Van Ginneken et al., 2012; Cordier and Folco, 2014; Noguchi et al., 2015) although the relative contribution from each source remains hotly debated (Brownlee, 2001; Plane, 2012).

Because unmelted micrometeorites (UMMs) retain mineral phases that formed prior to atmospheric entry, their study provides direct insights into the astrophysical conditions operating during the early solar system (Klöck et al., 1989; Beckerling and Bischoff, 1995; Greshake et al., 1996) and the geological history of their parent bodies (Genge et al., 1997; Engrand and Maurette, 1998; Suttle et al., 2019). Despite the advantages of studying UMMs, there are far fewer detailed investigations on unmelted particles than on cosmic spherules. This is primarily due to the limited number of MM collection sites that preserve highly friable UMMs as well as the difficulty in identifying UMMs within terrestrial sediment and the challenges associated with analysing small, scientifically valuable materials. Indeed, most MMs fall within the size range 50–300 μm making their collection practically challenging (Maurette et al., 1991; Brownlee et al., 1997; Taylor et al., 1998, 2000; Yada et al., 2004; Prasad et al., 2013, 2018).

Of the extraterrestrial dust collected from various environments (e.g., Antarctica, deep-sea sediments, and in the case of the smaller interplanetary dust particles [IDPs] the stratosphere) it is estimated that roughly half survive without significant melting (Love and Brownlee, 1991; Maurette et al., 1991; Taylor et al., 1998; Yada et al., 2004; Rudraswami et al., 2016a; Prasad et al., 2018; Rojas et al., 2021; Rudraswami et al., 2020a). The degree of atmospheric entry heating is a function of multiple variables. Numerical modelling demonstrates that particles with low entry velocities (<16 km s^{-1}) and low entry angles (<10°) are heated for longer times but at lower peak temperatures. These grains are therefore more likely to be unmelted (Love and Brownlee, 1991; Carrillo-Sánchez et al., 2015). Additionally smaller MMs (<300 μm) preferentially survive as compared to larger ones. This is reflected in the dramatic change in the ratio of unmelted-to-melted particles at different size fractions, as demonstrated empirically by Taylor et al. (2007) from the South Pole Water Well (SPWW) collection and from comparison between different MM collections (e.g., Table 1 in Suttle and Folco, 2020). Furthermore, the chemical composition and mineralogy of dust can also strongly affect survival rates, notably where the thermal decomposition of phyllosilicate in hydrated dust grains acts as an efficient heat sink, resulting in high thermal gradients (>200Kμm^{-1}) and the retention of low core temperatures (Genge, 2006; Genge et al., 2017). By contrast, anhydrous particles, large dust grains (>300 μm) and particles that enter the Earth's resonance orbit with high entry velocity (>16kms^{-1}) and high entry angles (>10°) will experience significant heating and corresponding chemical and isotopic alteration (Love and Brownlee, 1991; Rudraswami et al., 2016b).

Atmospheric entry heating not only affects the chemical composition but also the bulk O-isotope composition of MMs (e.g., Yada et al., 2005; Suavet et al., 2010; Cordier and Folco, 2014; Van Ginneken et al., 2017; Rudraswami et al., 2019, 2020b; Suttle et al., 2020; Goderis et al., 2020). This can potentially alter the O-isotopic composition of melted cosmic spherules. An alternative approach is therefore to use spatially resolved isotopic analysis to avoid MM mesostasis (defined as phases that formed during atmospheric entry via melting and recrystallization) and instead analyse only relict[1] mineral grains held either within unmelted particles (Greshake et al., 1996; Engrand et al., 1999; Gounelle et al., 2005; Matrajt et al., 2006) or cosmic spherules (Yada et al., 2005; Suavet et al., 2011; Rudraswami et al., 2015, 2016a). Relict phases are expected to largely retain their pre-atmospheric O-isotope composition and allow the origin of MM to be established.

In the present work, we focus on unmelted coarse-grained micrometeorites (CgMMs) and relict-grain-bearing (RGB) porphyritic (PO) cosmic spherules. We have performed 95 in-situ oxygen isotope analyses (using an ion microprobe [Cameca IMS-1270 at the CRPG-Nancy, France]) on 37 particles. Our study population includes olivine-bearing CgMMs presenting either as single mineral grains or mineral clusters. We also analysed spinel-

[1] Note, use of "relict grain" with respect to chondrule silicates is distinct from the use of "relict grain" often used in studies of MMs. In MM papers relict is often used to draw a distinction between grains that survived unmelted (relicts) and mesostasis material that melted, homogenised and recrystallized during atmospheric entry. By contrast, when referring to chondrule histories, relict grains refer to grains that survived through episodes of chondrule melting and crystallization.

Table 1
Particle classifications for the 37 micrometeorites analysed in this study. Abbreviations are Ol. = olivine, Px. = pyroxene, Mesos. = mesostasis, Sp. = spinel, Chr. = chromite, Sul. = Fe-sulphides and Fg-matrix = fine-grained matrix.

ID	Particle ID	Classification	Sub-classification	Additional texture notes	Exposed area (μm)	Main mineralogy	Petrographic description
1	SP005-P29	Unmelted	Coarse-grained	Grain cluster	102 × 80	Ol., Mesostasis	Small rounded anhydrous silicates and metal embedded in a silicate glass. Glass contains submicron Fe-oxides & Ol.
2	SP005-P109	Unmelted	Coarse-grained	Grain cluster	164 × 117	Ol., Mesostasis	Well-developed igneous rim (20−100 μm) enclosing relict forsterite grain cluster. (Ol. contains polikolitic kamacite beads).
3	SP005-P128	Unmelted	Coarse-grained	Grain cluster	108 × 95	Ol., Px., Mesos.	Well-developed igneous rim (∼20 μm) enclosing relict forsterite grain cluster. (Ol. contains polikolitic kamacite beads).
4	SP005-P261	Unmelted	Coarse-grained	Grain cluster	44 × 30	Ol.	Four large irregular-shaped forsterite grains enclosed by a thin (<3μm) igneous rim.
5	SP005-P372	Unmelted	Coarse-grained	Grain cluster	107 × 80	Ol.	Particle dominated by a large forsterite grain w/. evidence of subgrain formation. Weak discontinous magnetite rim on one edge
6	SP005-P727	Unmelted	Coarse-grained	Grain cluster	85 × 67	Ol., Mesostasis	Large forsterite grain cluster and attached fine-grained groundmass. No igneous or magnetite rims
7	SP005-P728	Unmelted	Coarse-grained	Grain cluster	115 × 103	Ol., Mesostasis	Well-developed igneous rim (10−20 μm) enclosing relict forsterite grain cluster. (Ol. contains polikolitic kamacite beads).
8	SP005-P1035	Unmelted	Coarse-grained	Grain cluster	139 × 100	Ol., Mesostasis	Rounded forsterite grains embedded in silicate glass (glass affected by dissolution), core enclosed by a fine-grained rim.
9	SP005-P1162	Unmelted	Coarse-grained	Grain cluster	109 × 80	Ol.	Continuous igneous rim (<20 μm) enclosing relict forsterite grain cluster. (Ol. contains polikolitic kamacite beads).
10	SP007-P253	Unmelted	Coarse-grained	Grain cluster	165 × 108	Ol., Px., Mesos.	Irregular-shaped particle, forsterite grain cluster with interstitial silicate glass & rare metal droplets. Mantled by igneous rim
11	SP005-P160	Unmelted	Coarse-grained	Grain cluster	146	Ol., Mesostasis	Rounded forsterite grain cluster with interstitial silicate glass & metal droplets, mantled by a thin igneous rim.
12	SP005-P1042	Unmelted	Coarse-grained	Single mineral	78 × 58	Ol., Mesostasis	Large anhedral forsterite grain mantled by an igneous rim
13	SP005-P339	Unmelted	Coarse-grained	Single mineral	85 × 55	Ol.	Subrounded olivine grain w/. partial magnetite rim. Subsolidus oxidation precipitated magnetite crystals near grain's margin
14	SP005-P730	Unmelted	Coarse-grained	Single mineral	150 × 88	Ol.	Rounded olivine grain w/. subgrain formation and penetrating melt veins
15	SP005-P743	Unmelted	Coarse-grained	Single mineral	185 × 104	Ol.	Rounded olivine grain w/. thin continuous igneous rim
16	SP005-P930	Unmelted	Coarse-grained	Single mineral	186 × 119	Ol.	Subrounded olivine grain w/. Subsolidus oxidation precipitated magnetite crystals near grain's margin. Penetrating melt veins
17	SP005-P1029	Unmelted	Coarse-grained	Single mineral	103 × 74	Ol.	Subrounded olivine grain w/. Subsolidus oxidation precipitated magnetite crystals near grain's margin. Penetrating melt veins
18	SP007-P95	Unmelted	Coarse-grained	Single mineral	177 × 115	Ol., Fe-oxides	Subrounded olivine grain w/. Discontinuous igneous rim & oxidised metal bead
19	SP007-P185	Unmelted	Coarse-grained	Single mineral	93 × 63	Ol., Mesostasis	Subangular olivine grain w/. thick igneous rim on one side & penetrating melt veins
20	SP007-P270	Unmelted	Coarse-grained	Single mineral	80 × 64	Ol.	Subrounded olivine grain w/. Subsolidus oxidation precipitated magnetite crystals near grain's margin.

21	SP005-P167	Scoriaceous	Coarse-grained	Grain cluster	160 × 97	Ol., Sul., Metal	Several large rounded relict forsterite grains with normal zonation (neo-formed Fe-rich ol. rims) embedded in mesostasis.
22	SP005-P522	Unmelted	Coarse-grained	Spinel-bearing	92	Ol., Sp.	Rounded olivine grain enclosing a ~ 20 µm diameter spinel crystal. Mantled by a paired igneous & magentite rim.
23	SP005-P392	Unmelted	Coarse-grained	Spinel-bearing	132	Ol., Sp.	Rounded olivine grain containing metal droplets and a small (~15 µm diameter) spinel crystal. Mantled by an igneous rim.
24	SP005-P583	Cosmic spherule	PO (RGB)	Spinel-bearing	84	Ol., Sp., Mesos.,	A single, large (~20x40 µm) spinel grain w/. overgrowths of Fe-oxides embedded in a silicate glass.
25	SP005-P440	Cosmic spherule	PO (RGB)	Spinel-bearing	80	Ol., Sp., Mesos.	PO spherule w/. Two anhedral spinel grains.
26	SP007-P164	Cosmic spherule	PO (RGB)	Spinel-bearing	54	Ol., Sp., Mesos.	Single large relict spinel grain w/. Overgrowths of neoformed olivine embedded in silicate glass
27	SP006-P88	Cosmic spherule	PO (RGB)	Spinel-bearing	89	Ol., Sp., Mesos.	Large off-centre vesicle and fine-grained crystalline mesostasis. A single anhedral relict spinel grain survives
28	SP006-P102	Cosmic spherule	PO (RGB)	Spinel-bearing	98	Ol., Sp., Mesos.	Particle transitional between ScMM and a cosmic spherule. A single relict spinel grain survives.
29	SP005-P124	Cosmic spherule	PO (RGB)	-	119	Ol., Metal, Mesos.	Relict forsterite grains w/. Poorly defined margins (partially melted). ~ 50% mesostasis surrounds relict core
30	SP005-P302	Cosmic spherule	PO (RGB)	-	131 × 106	Ol., Mesostasis	Absence of igneous/magnetite rims indicates a cosmic spherule. Core dominated by large anhedral forsterite in mesostasis glass
31	SP005-P351	Cosmic spherule	PO (RGB)	-	104	Ol.	Poryhritic cosmic spherule containing relict fosterite grains with Fe-rich rims that formed during atm. entry.
32	SP005-P586	Cosmic spherule	PO (RGB)	-	110 × 70	Ol., Mesostasis	Single large irregular-shaped anhedral forsterite grain held in mesostasis
33	SP005-P700	Cosmic spherule	PO (RGB)	-	98 × 41	Ol., Glass	Many rounded relict forsterite grains of uniform BSE contrast embedded in mesostasis glass. Magnetites growing on relict grains
34	SP005-P703	Cosmic spherule	PO (RGB)	-	105 × 103	Ol., Glass	Several small rounded relict forsterite grains of uniform BSE contrast embedded in mesostasis glass.
35	SP005-P791	Cosmic spherule	PO (RGB)	-	95 × 65	Ol., Chr., Glass	Two large anhedral forsterite grains & one chromite grain embedded in mesostasis glass.
36	SP005-P1070	Cosmic spherule	PO (RGB)	-	90	Px.,	Rounded forsterite grains & abundant Fe-Ni metal beads embedded in mesostasis glass.
37	SP007-P257	Scoriaceous	Fine-grained	-	166 × 124	Fg-matrix, sul., Ol.	Relict fine-grained matrix. Matrix is dark (Mg-rich) & contains submicron sulphides and small relict Ol. grains

bearing cosmic spherules. As a result, the main target phases investigated are olivine, spinel and, for context surrounding MM mesostasis.

2. OXYGEN ISOTOPES IN CHONDRITIC MATERIALS

Chondritic meteorites are isotopically heterogeneous (Clayton et al., 1977; Jones et al., 2004; Ushikubo et al., 2012; Marrocchi et al., 2018b). Their respective components display distinct and well-characterised O-isotope ranges. Chondrules and refractory inclusions (Ca-, Al-rich inclusions [CAIs] and amoeboid olivine inclusions [AOAs]) have compositions that plot either on or close to the carbonaceous chondrite anhydrous mineral (CCAM) line (Clayton and Mayeda, 1999) or the Primitive Chondrule Mineral (PCM) line (Ushikubo et al., 2012). These lines have slopes of approximately 1 in $\delta^{18}O$–$\delta^{17}O$ isotope space (in detail: ~0.94 and ~ 1 for the CCAM and PCM lines, respectively). They reflect a fundamental mass-independent process that was operating in the solar nebula as the first solid phases condensed to form CAIs and were later followed by flash melting and cooling of solid precursors to form chondrules.

This process can be interpreted as mixing between ^{16}O-rich and ^{16}O-poor reservoirs or partial exchange of oxygen between solar-like ^{16}O-rich refractory silicates and a ^{16}O-poor nebula gas (either SiO or SiO_2 gas) during transient chondrule heating, melting and recycling events (e.g., Yu et al., 1995; Young and Russell, 1998; Bridges et al., 1999; Jones et al., 2004; Chaussidon et al., 2008; Rudraswami et al., 2011; Ushikubo et al., 2012; Tenner et al., 2013, 2015, 2018; Marrocchi and Chaussidon, 2015; Marrocchi et al., 2018a, b; Simon et al., 2019; Bodénan et al., 2020; Krot et al., 2020). Individual chondrules often contain modest O-isotope variation (less than a few ‰). However, relict grains with isotopically light values (potentially as low as $\delta^{18}O$–$\delta^{17}O \approx -50‰$) occur at low abundances. They are interpreted as earlier generations of chondrule silicates, some of which appear to have been derived from CAI material. Meanwhile, heavier isotopic compositions, found in most chondrule silicates plot along the slope-1 (CCAM or PCM) lines and close to the Terrestrial Fractionation Line (TFL). Their compositions indicate later generation crystals formed by progressive melting and interaction with nebula gases (Krot et al., 2006; Chaussidon et al., 2008; Chaumard et al., 2018).

By contrast, the fine-grained matrix in chondrites as well as any secondary minerals (formed by parent body processes) tend to have O-isotope compositions that plot off the slope-1 lines, shifted to heavier (^{16}O-poor) compositions. These phases instead define shallower lines with slopes > 0.52 and < 1 in $\delta^{18}O$–$\delta^{17}O$ isotope space (Rowe et al., 1994; Clayton and Mayeda, 1999; Yurimoto et al., 2008; Ireland et al., 2020). They are generally interpreted as evidence of parent body alteration resulting in the equilibration of ^{16}O-rich anhydrous silicates (within chondrules/CAIs/AOAs) with a ^{16}O-poor, isotopically heavy water-ice component (e.g., Clayton and Mayeda, 1999; Chaumard et al., 2018).

Spinel is a crucial refractory mineral in early solar system objects, often found as a component of CAIs and, to a lesser extent, in chondrules (Maruyama et al., 1999; Maruyama and Yurimoto, 2003; Rudraswami et al., 2011). It melts at high temperature > 2000 °C and is also relatively resistant to later parent body alteration (Greenwood et al., 1994). Primary spinel grains ($MgAl_2O_4$) are rarely found in MMs (Taylor et al., 2012). They are distinct from the abundant small iron-rich spinel grains that form in MMs during atmospheric entry (resulting in the formation of magnetite rims on unmelted and scoriaceous MMs; Toppani et al., 2001). Owing to their low abundance only a few primary spinels have been analyzed (Taylor et al., 2012). We also study relict olivine grains, they are likewise resistant to O-isotopic exchange during atmospheric entry due to relatively slow diffusion kinetics and relatively large grain sizes (Yada et al., 2005). Detailed in-situ O-isotope analyses of UMMs (and especially spinel-bearing particles) are limited in literature (Engrand et al., 1999; Gounelle et al., 2005; Matrajt et al., 2006; Rudraswami et al., 2015, 2016a; Dobrică et al., 2019), as such the current study aims to provide new data on their origin, formation and relationship to phases found in primitive chondrites.

3. SAMPLE COLLECTION

The MMs were vacuumed from the bottom of the South Pole water well (SPWW), ~100 m beneath the snow surface. The well with a diameter of ~24 m and depth of ~15 m has a potential to retrieve a large source of preserved extraterrestrial particles with low terrestrial contamination. The depositional age of the MMs studied (mounts SP005, SP006 and SP007) was between ~800 and 1100 A.D (Taylor et al., 2007). The MMs were mounted in epoxy and then polished to expose their approximate maximum interior surface area. The particles were examined using back-scattered electron (BSE) imaging to facilitate classification and the identification of mineral phases following the methodology of Genge et al. (2008). The oxygen isotope and chemical composition of target phases in selected MMs were subsequently analysed. Our study population includes 37 particles (Table 1), comprising a mix of unmelted/scoriaceous CgMMs ($n = 23$) and RGB porphyritic (PO) cosmic spherules ($n = 13$). In addition, we analysed a single scoriaceous fine-grained micrometeorite (FgMM) (SP007-P257).

4. ANALYTICAL TECHNIQUES

4.1. Electron microscopy

The high-resolution back-scattered electron images (BSE) of carbon-coated polished MM interiors were obtained by scanning electron microscope (SEM, JEOL JSM 5800LV) equipped with an Oxford Instruments energy dispersive spectrometer (EDS, ISIS-300 at National Institute of Oceanography, Goa) and using the INCA software. Backscattered electron images were used to classify particles and identify phases for oxygen isotope analysis. Supporting geochemical data on selected phases were

Table 2
The oxygen isotope compositions of mineral phases and mesostasis collected by ion microprobe on 37 MMs. The oxygen isotope values are expressed in ‰ (relative to VSMOW).

No.	Particle ID	Classification	Subclassification	Spot#	Phase	Mg#	$\delta^{17}O$	2σ	$\delta^{18}O$	2σ	$\Delta^{17}O$	2σ
1	SP005-P29	Unmelted	Coarse-grained	1	Olivine	80.1	2.9	0.3	5.8	0.8	−0.1	0.6
				2	Olivine	79.4	2.3	0.3	6.5	0.8	−1.1	0.5
				3	Olivine	76.6	3.0	0.4	6.1	0.8	−0.2	0.6
2	SP005-P109	Unmelted	Coarse-grained	1	Olivine	98.3	−3.7	0.4	0.4	0.7	−3.9	0.5
				2	Olivine	98.5	−8.7	0.4	−6.4	0.8	−5.3	0.6
				3	Olivine	89.2	−9.4	0.4	−6.6	0.7	−6.0	0.5
				4	Olivine	98.1	−7.6	0.4	−3.8	0.7	−5.6	0.6
				5	Mesostasis	51.6	−6.3	0.4	−3.6	0.7	−4.5	0.5
3	SP005-P128	Unmelted	Coarse-grained	4	Mesostasis	43.3	2.1	0.4	7.9	0.7	−2.0	0.5
4	SP005-P261	Unmelted	Coarse-grained	1	Olivine	98.8	−4.0	0.4	2.4	0.7	−5.2	0.6
				2	Olivine	98.7	−3.2	0.4	4.0	0.7	−5.3	0.5
				3	Olivine	96.0	−5.3	0.4	−0.8	0.9	−4.9	0.6
5	SP005-P372	Unmelted	Coarse-grained	1	Olivine	80.5	3.3	0.4	5.2	0.5	0.6	0.5
				2	Olivine	81.3	3.5	0.3	5.7	0.6	0.6	0.4
				3	Olivine	80.8	2.4	0.3	3.2	0.6	0.7	0.4
6	SP005-P727	Unmelted	Coarse-grained	1	Olivine	63.1	2.4	0.3	3.3	0.6	0.7	0.4
				2	Olivine	61.6	2.9	0.3	4.6	0.5	0.5	0.4
7	SP005-P728	Unmelted	Coarse-grained	1	Olivine	97.3	−4.1	0.4	−1.7	0.5	−3.2	0.5
				2	Olivine	97.1	−3.2	0.4	−0.9	0.6	−2.7	0.5
8	SP005-P1035	Unmelted	Coarse-grained	1	Olivine	99.1	−8.7	0.4	−5.2	0.7	−6.0	0.5
				2	Olivine	99.0	−7.4	0.4	−2.3	0.7	−6.2	0.6
9	SP005-P1162	Unmelted	Coarse-grained	1	Olivine	90.1	−5.0	0.4	−5.8	0.9	−1.9	0.6
				2	Olivine	92.3	−5.0	0.5	−3.6	0.9	−3.1	0.7
				3	Olivine	76.8	−3.6	0.4	−0.8	0.8	−3.2	0.6
10	SP007-P253	Unmelted	Coarse-grained	1	Low-Ca Px.	96.4	−8.3	0.5	−5.9	0.6	−5.3	0.6
				2	Olivine	86.0	−6.4	0.4	−4.5	0.6	−4.1	0.5
				3	Olivine	98.0	−6.1	0.4	−3.4	0.6	−4.4	0.6
				4	Olivine	98.8	−6.4	0.4	−3.8	0.7	−4.4	0.6
11	SP005-P160	Unmelted	Coarse-grained	1	Olivine	99.4	−10.0	0.4	−7.6	0.6	−6.1	0.5
				2	Olivine	99.3	−11.0	0.4	−8.7	0.8	−6.4	0.6
				3	Olivine	99.2	−11.4	0.4	−9.6	0.8	−6.4	0.6
				4	Olivine	99.2	−10.0	0.4	−7.3	0.6	−6.2	0.5
				5	Olivine	99.2	−11.0	0.3	−9.1	0.7	−6.2	0.5
12	SP005-P1042	Unmelted	Coarse-grained	1	Olivine	59.5	−0.6	0.4	2.9	0.6	−2.2	0.5
				2	Olivine	61.5	−0.5	0.3	2.0	0.5	−1.5	0.4
13	SP005-P339	Unmelted	Coarse-grained	1	Olivine	72.4	3.1	0.4	6.0	0.9	0.0	0.6
				2	Olivine	71.9	2.7	0.5	4.7	0.8	0.3	0.6
14	SP005-P730	Unmelted	Coarse-grained	1	Olivine	80.3	2.7	0.4	5.5	0.6	−0.1	0.5
				2	Olivine	80.4	3.2	0.4	3.8	0.5	1.3	0.5
15	SP005-P743	Unmelted	Coarse-grained	1	Olivine	97.8	−3.0	0.4	0.6	0.7	−3.3	0.5
				2	Olivine	97.7	−2.7	0.4	0.2	0.6	−2.8	0.5
16	SP005-P930	Unmelted	Coarse-grained	1	Olivine	71.5	−4.3	0.4	0.1	0.5	−4.4	0.5
				2	Olivine	68.5	−3.7	0.3	−0.1	0.5	−3.6	0.4
17	SP005-P1029	Unmelted	Coarse-grained	1	Olivine	68.2	0.7	0.4	3.1	0.5	−0.9	0.4
				2	Olivine	67.1	1.4	0.3	4.4	0.6	−1.0	0.5
18	SP007-P95	Unmelted	Coarse-grained	1	Olivine	62.6	3.1	0.4	5.0	0.7	0.5	0.6
				2	Olivine	62.0	3.2	0.5	4.1	0.7	1.1	0.6
				3	Olivine	61.4	3.0	0.5	4.9	0.6	0.5	0.6
19	SP007-P185	Unmelted	Coarse-grained	1	Olivine	71.1	3.0	0.4	3.6	0.8	1.1	0.6
20	SP007-P270	Unmelted	Coarse-grained	1	Olivine	62.0	−7.4	0.4	−4.4	0.6	−5.2	0.5
				2	Olivine	60.9	−6.7	0.4	−4.0	0.6	−4.7	0.5
21	SP005-P167	Scoriaceous	Coarse-grained	1	Olivine	90.1	1.4	0.3	4.3	0.6	−0.8	0.4
22	SP005-P522	Unmelted	Coarse-grained	1	Spinel	98.3	−9.6	0.4	−8.2	1.0	−5.3	0.7
				2	Olivine	99.5	−7.7	0.4	−3.7	0.9	−5.8	0.6
				3	Olivine	99.3	−7.7	0.3	−5.2	0.6	−5.0	0.5
23	SP005-P392	Unmelted	Coarse-grained	1	Spinel	97.1	−6.9	0.4	−4.1	1.1	−4.7	0.7
				2	Spinel	96.2	−7.2	0.5	−5.3	1.0	−4.4	0.7
				3	Olivine	98.9	−4.7	0.4	0.1	0.7	−4.8	0.5
				4	Olivine	98.9	−4.4	0.4	0.7	0.6	−4.7	0.5

24	SP005-P583	Cosmic spherule	PO (RGB)	1	Spinel	78.3	−34.4	0.5	−30.8	1.0	−18.3	0.7
				2	Spinel	76.4	−32.1	0.5	−29.1	1.1	−16.9	0.8
				3	Mesostasis	51.2	−10.4	0.4	−0.3	0.8	−10.2	0.6
				4	Mesostasis	38.7	−11.7	0.4	−3.3	0.8	−10.0	0.6
25	SP005-P440	Cosmic spherule	PO (RGB)	1	Spinel	98.4	−18.1	0.7	−12.9	1.0	−11.4	0.8
				2	Spinel	89.2	−8.6	0.4	0.3	1.1	−8.7	0.7
				3	Spinel	71.8	−0.9	0.5	11.0	0.9	−6.6	0.7
				4	Mesostasis	26.6	−6.4	0.3	8.7	0.6	−10.9	0.5
26	SP007-P164	Cosmic spherule	PO (RGB)	1	Spinel	93.2	−13.7	0.4	−5.2	1.0	−11.0	0.6
				2	Spinel	95.0	−20.0	0.3	−12.9	0.8	−13.3	0.5
27	SP006-P88	Cosmic spherule	PO (RGB)	1	Spinel	93.1	−22.3	0.5	−16.0	0.8	−13.9	0.6
				2	Olivine	99.4	−12.6	0.5	−6.0	0.9	−9.5	0.7
28	SP006-P102	Cosmic spherule	PO (RGB)	1	Mesostasis	52.9	11.4	0.4	22.0	1.0	0.0	0.7
				2	Mesostasis	99.6	15.1	0.5	30.9	0.6	−1.0	0.6
29	SP005-P124	Cosmic spherule	PO (RGB)	1	Olivine	71.3	−1.3	0.4	1.3	0.8	−2.0	0.5
				2	Olivine	98.3	−8.5	0.4	−4.7	0.7	−6.0	0.5
				3	Olivine	96.3	−6.9	0.3	−3.3	0.6	−5.1	0.5
30	SP005-P302	Cosmic spherule	PO (RGB)	1	Olivine	76.3	−0.1	0.4	2.6	0.7	−1.5	0.5
				2	Olivine	76.1	−4.0	0.5	−1.5	0.6	−3.2	0.6
31	SP005-P351	Cosmic spherule	PO (RGB)	1	Olivine	92.8	0.2	0.4	4.3	0.6	−2.0	0.5
				2	Olivine	99.3	−28.2	0.4	−22.8	0.7	−16.3	0.6
				3	Mesostasis	97.7	3.1	0.3	9.8	0.5	−2.0	0.4
32	SP005-P586	Cosmic spherule	PO (RGB)	1	Mesostasis	56.1	2.9	0.4	6.9	0.6	−0.7	0.5
33	SP005-P700	Cosmic spherule	PO (RGB)	1	Olivine	60.3	1.1	0.3	2.5	0.6	−0.2	0.4
				2	Olivine	61.9	2.9	0.3	7.5	0.5	−1.0	0.4
				3	Olivine	59.6	1.9	0.4	6.1	0.6	−1.2	0.5
34	SP005-P703	Cosmic spherule	PO (RGB)	1	Olivine	64.9	0.0	0.4	2.6	0.7	−1.3	0.6
				2	Olivine	65.2	1.1	0.5	2.6	0.6	−0.3	0.6
35	SP005-P791	Cosmic spherule	PO (RGB)	1	Olivine	67.0	2.8	0.3	3.0	0.6	1.2	0.4
				2	Olivine	66.0	2.8	0.4	2.9	0.5	1.3	0.5
36	SP005-P1070	Cosmic spherule	PO (RGB)	1	Low-Ca Px.	94.3	−5.8	0.3	−4.0	0.9	−3.7	0.6
				2	Low-Ca Px.	92.3	−5.8	0.4	−2.8	0.6	−4.4	0.5
37	SP007-P257	Scoriaceous	Fine-grained	1	Fg-matrix	68.2	12.8	0.5	23.8	0.8	0.4	0.6
				2	Fg-matrix	53.2	8.8	0.7	17.8	1.0	−0.5	0.9
				3	Fg-matrix	71.4	14.2	0.9	23.7	1.8	1.9	1.2
				4	Mesostasis	51.3	10.0	0.7	16.9	0.8	1.2	0.8

acquired using a Cameca SX Five Electron Probe Micro Analyzer (EPMA at National Institute of Oceanography, Goa) fitted with four wavelength-dispersive x-ray spectrometers. The chemical analyses of particles under electron probe were performed at an accelerating voltage of 15 kV, a beam current of ~ 12 nA and a beam width of ~ 1–2 µm. Further analytical details for the EPMA work are given in Rudraswami et al. (2015). Based on the preliminary electron microscopy characterisation, we selected 95 spots, mostly on olivine and spinel phases for in-situ O-isotope analysis. Chemical data for all phases analysed by EPMA are given in Supplementary Material (Appendix A).

4.2. Ion microprobe analyses

Triple O-isotope analyses were acquired using a secondary ion mass spectrometer – the Cameca IMS-1270 instrument located at CRPG-Nancy, France. A detailed description of the analytical method was previously reported in Rudraswami et al. (2019). This study used a focused Cs^+ ion beam with a primary current of ~ 1 nA and beam size of ~ 5 µm at the sample surface. Analyses achieved a mass resolving power of ~2500 for ^{16}O and ^{18}O ions, while an improved resolving power of ~7000 was required for the measurement of ^{17}O ions to avoid measuring the interference of $^{16}OH^-$ on the ^{17}O ion peak. Secondary ion signals were measured using Faraday cups for ^{16}O and ^{18}O ions, while an electron multiplier was used for ^{17}O. The instrumental mass fractionation for olivine and spinel grains were corrected using terrestrial standards (San Carlos olivine and Burma spinel, respectively). There are small matrix effects in measured olivine grains arising due to variable chemical compositions of natural samples. However, the magnitude of these effects are small and, in most instances the Mg content of target minerals were close to the composition of the analytical standard (Isa et al. 2017). We report O-isotope data in standard δ notation. Ratios of $^{17}O/^{16}O$ and $^{18}O/^{16}O$ are given as $\delta^{17,18}O = [(^{17,18}O/^{16}O)_{sample} / (^{17,18}O/^{16}O)_{SMOW}) - 1] \times 1000$ (‰). $\Delta^{17}O$, which represents the deviation from the terrestrial fractionation has been calculated as $\Delta^{17}O = \delta^{17}O - 0.52 \times \delta^{18}O$. The error reported was determined by the reproducibility of multiple standard analyses for $\delta^{17,18}O$ propagated to errors in individual measurements. All errors in this study are quoted to the 2σ level (Table 2) and range between 0.3‰ and 0.9‰ for $\delta^{17}O$, between 0.5‰ and 1.8‰ for $\delta^{18}O$ and between 0.4‰ and 1.2‰ for $\Delta^{17}O$. Micrometeorites were mounted close to the centre

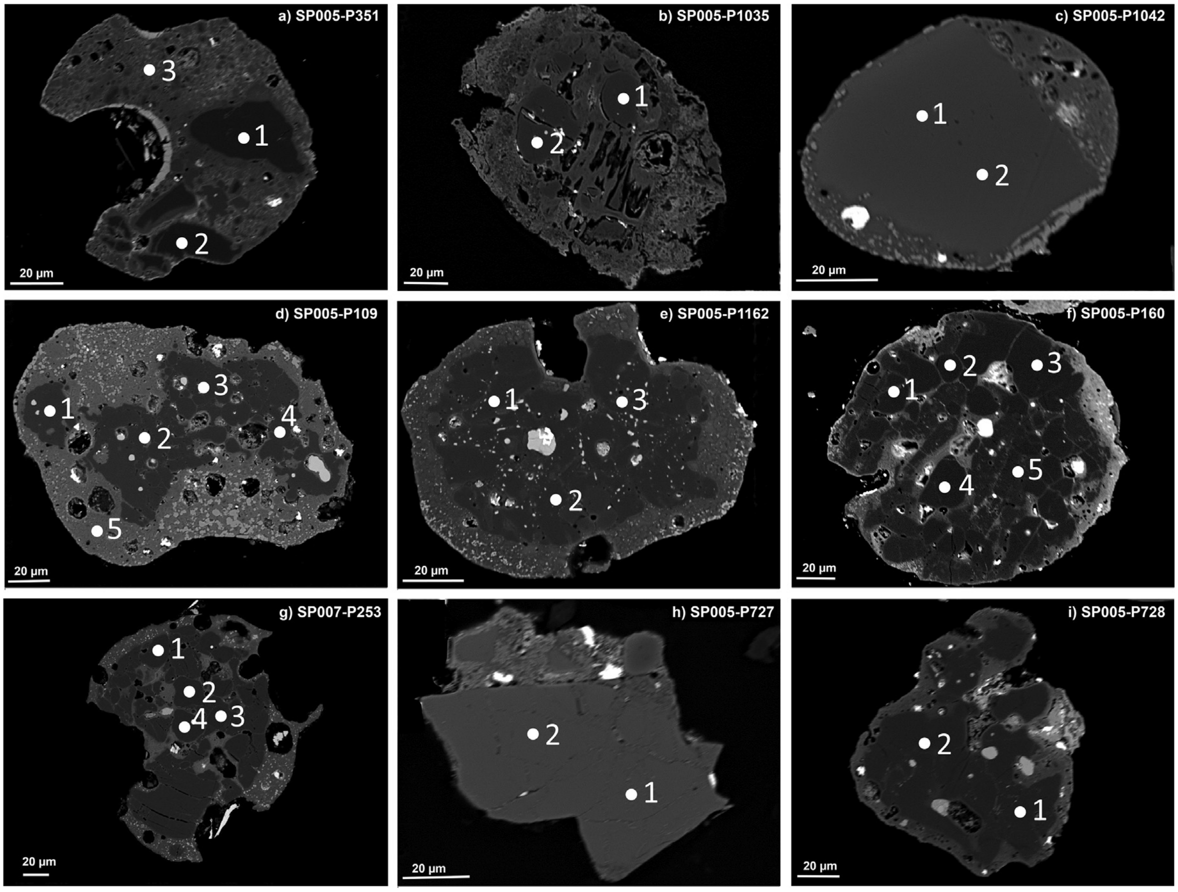

Fig. 1. Representative backscattered electron (BSE) images of CgMM and relict-grain bearing PO cosmic spherules analysed in this study. (a) SP005-P351, (b) SP005-P1035, (c) SP005-P1042, (d) SP005-P109, (e) SP005-P1162, (f) SP005-P160, (g) SP007-P253, (h) SP005-P727, and (i) SP005-P728. Petrographic and chemical studies were done on some particles by Rudraswami et al. (2015), but not for oxygen isotope studies. The white circle with the number indicate the spot of oxygen isotope analyses and the corresponding data is provided in Table 2.

of their polished block to avoid large instrumental mass fractionation effects arising between samples and standards (Kita et al., 2009). For each sample one or more spots were carefully selected for ion microprobe analysis depending on the size of mineral surface (Supplementary Material-Appendix B).

5. RESULTS

5.1. Petrographic details of MMs

Most of the CgMMs (examples shown in Fig. 1) have spherical shapes and, in section view, have a centrally located rounded grain cluster composed predominantly of forsterite grains (Fo59.5–99.5, median = Fo81.1) with/or without minor pyroxene, Fe-Ni metal (as kamacite), Fe-sulphides and, in rare instances silicate glass of pre-atmospheric origin (**e.g.,** SP005-P1035 [Fig. 1b]). These unmelted cores are mantled by a well-developed layer of mesostasis, termed an igneous rim (Genge, 2006). In addition, most of the CgMMs have an outer discontinuous shell of magnetite rim on the particle exterior (Toppani et al., 2001). Both igneous rims and magnetite rims are extensively documented in the literature and form during atmospheric entry by partial melting. As such igneous and magnetite rims are routinely used as diagnostic evidence in the classification of unmelted/scoriaceous MMs, as distinct from cosmic spherules (Genge, 2006; Genge et al., 2008; van Ginneken et al., 2012). They are also useful guidelines which visually mark the boundary between the particle's melted exterior and its unmelted (but thermally altered) interior (Genge, 2006). By definition cosmic spherules have experienced more thermal processing than the unmelted CgMMs (Genge et al., 2008). They lack igneous/magnetite rims and are instead dominated by mesostasis (which may take the form of quench-cooled Ca-rich glass, euhedral Fe-rich olivine phenocrysts, magnetite dendrites and/or a nanocrystalline groundmass of Fe-rich olivine). However, relict grains can be confidently identified by their anhedral shapes, darker Z-values in BSE images (indicating more Mg-rich compositions), minor element compositions enriched in Cr, Mn and Ca and by the presence of normal

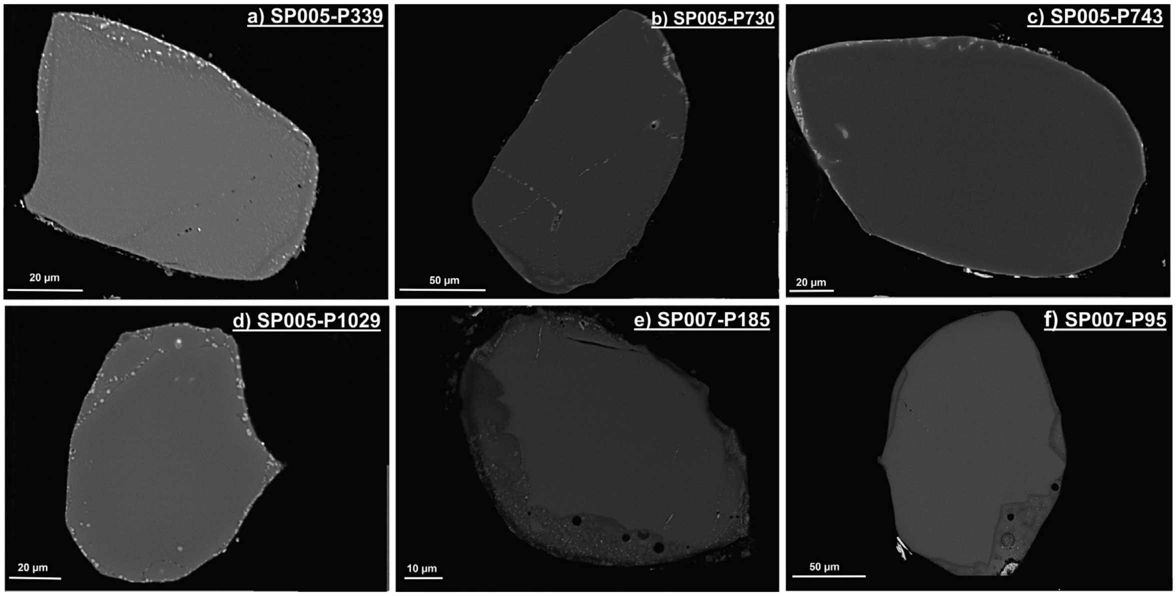

Fig. 2. Representative backscattered electron (BSE) images of single mineral MMs analysed using ion microprobe. Olivine is the dominant mineral and is analysed for oxygen isotope studies. (a) SP005-P339, (b) SP005-P730, (c) SP005-P743, (d) SP005-P1029, (e) SP007-P185, and (f) SP005-P95. Only petrographic and chemical studies were done on some particles by Taylor et al. (2012) (d) and Rudraswami et al. (2015) (a, b, c, d), but not for oxygen isotope studies.

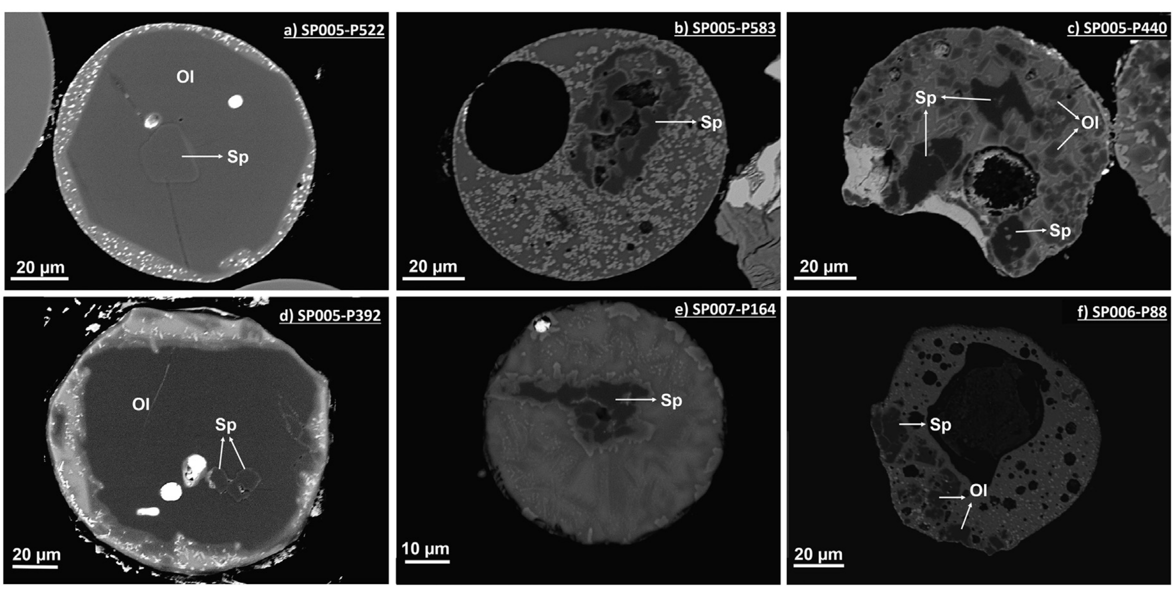

Fig. 3. The backscattered electron (BSE) images of spinel-bearing MMs analysed using ion microprobe are shown. Spinel is rarely found in MMs and is marked in BSE images along with olivine. (a) SP005-P522, (b) SP005-P583, (c) SP005-P440, (d) SP005-P392, (e) SP005-P164, and (f) SP005-P88. The abbreviation Sp. and Ol. stand for spinel and olivine, respectively. Only petrographic and chemical studies were done earlier by Taylor et al. (2012) and Rudraswami et al. (2015). Oxygen isotope analyses of spinel grains on SP005-P583 and SP005-P164 were done previously by Taylor et al. (2012) is repeated in the present study.

zonation (Fe-rich rims on Mg-rich cores) indicating growth of new Fe-rich olivine onto the margins of relict grains during atmospheric entry (Steele, 1992; Beckerling and Bischoff, 1995; Genge et al., 2008).

Nine of the CgMMs contain a single mineral grain (examples shown in Fig. 2). This is distinct from the "typical" CgMM texture that have multiple minerals. As a result, the single mineral MMs are treated somewhat separately in this manuscript and assigned their own subgroup: CgMM-SM. In all instances the mineral phase is forsterite. As with the typical CgMMs, the single mineral varieties also contain igneous and magnetite rims along their exteriors. In addition, some grains have a high density of submicron-sized Fe-oxide grains along their grain margins. These are magnetite crystals that formed during atmospheric entry by flash heating under an oxidizing regime, they can form either by sub-solidus oxidation of olivine, leading to the exsolution of magnetite (Cordier et al., 2018) or by melting and recrystallization (Blanchard and Cunningham, 1974). Finally, some of the CgMM-SM have thin melt veins that have penetrated in towards their cores – further evidence of thermal processing during atmospheric entry.

We also analysed eleven spinel inclusions from seven spinel-bearing MMs (two CgMMs and five PO cosmic spherules [examples shown in Fig. 3]). Spinel grains range in size from 10 to 40 μm and often appear as anhedral crystals either held inside a host olivine crystal (as in SP005-P522 [Fig. 3a]) or embedded directly within mesostasis (as in SP005-P583 [Fig. 3b]). In all instances spinels are Mg-Al varieties with stoichiometries approximated by $MgAl_2O_4$ and containing minor FeO (~0.8–15 wt.%) as well as trace of Cr_2O_3 (~0.2–2.0 wt.%) and TiO_2 (<0.1wt.%, except in SP007-P164).

One of the particles we analysed (SP007-P257) is an FgMM with a partially melted, scoriaceous texture. The core preserves relict fine-grained matrix with a relatively Mg-rich composition (Mg# varies between 68 and 71) and contains both Fe-sulphides and small Mg-rich anhydrous silicates. It therefore exhibits a C2 texture in the classification scheme of Van Schmus and Wood (1967), indicating its parent body was a hydrated carbonaceous chondrite (CC). The relict matrix is enclosed by a well-developed vesicular igneous rim and a thin but continuous magnetite rim.

5.2. O-isotope data

We performed 71 O-isotope analyses (Fig. 4) on anhydrous silicate grains, of these 68 were on forsterite grains and three were on low-Ca pyroxenes (Table 2). Except for a single grain (within particle SP005-P351 [Fig. 1a]) with a distinctly ^{16}O-rich composition (δ^{17}O: −28.2‰, δ^{18}O: −22.8‰ and Δ^{17}O: −16.3‰) all the anhydrous silicates fall within a narrow range in δ^{18}O–δ^{17}O isotope space. Their δ^{17}O values vary between −12.6‰ and +3.5‰, δ^{18}O values vary between −9.6‰ and +7.5‰ and Δ^{17}O values vary between −9.5‰ and +1.3‰ (Fig. 4). As such this population can be collectively considered as consistent with the trends defined by the primordial CCAM and PCM reference lines, although several individual data points are slightly mass fractionated off this trendline towards heavier values (Fig. 4).

Nine analyses plot slightly below the CCAM line, shifted to marginally more ^{16}O-poor values and many of the for-

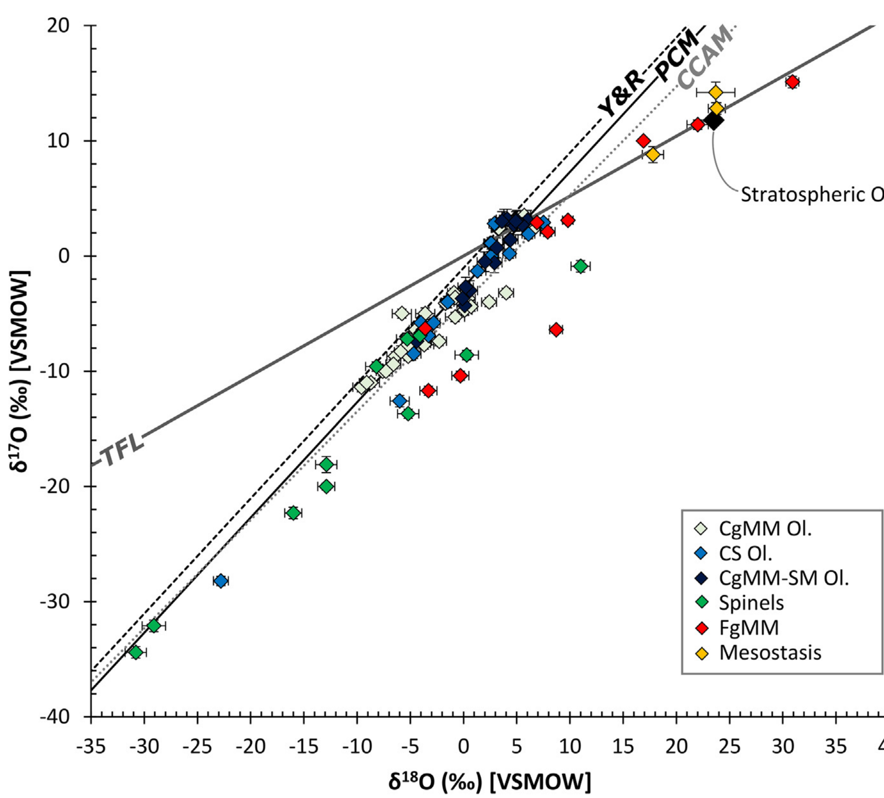

Fig. 4. All 95 O-isotope analyses collected in this study, plotted in δ^{18}O–δ^{17}O isotope space. Forsterite grains are shown in blue with different shades denoting olivine grains hosted within unmelted CgMMs (light blue), CgMM-SM (dark blue) and relict olivine grains held within a PO cosmic spherules (medium blue). Analyses on spinel grains are shown in green, analyses from the single FgMM are shown in yellow while analyses on mesostasis regions are shown in red. Error bars are reported at the 2σ level. We also show the CCAM line (Clayton et al., 1977), Y&R line (Young and Russell, 1998) and the PCM line (Ushikubo et al., 2012). Shaded regions mark the approximate domains occupied by reprocessed CAIs, chondrules within CCs (Tenner et al., 2018) and chondrules within OCs (Clayton et al., 1991; Kita et al., 2010).

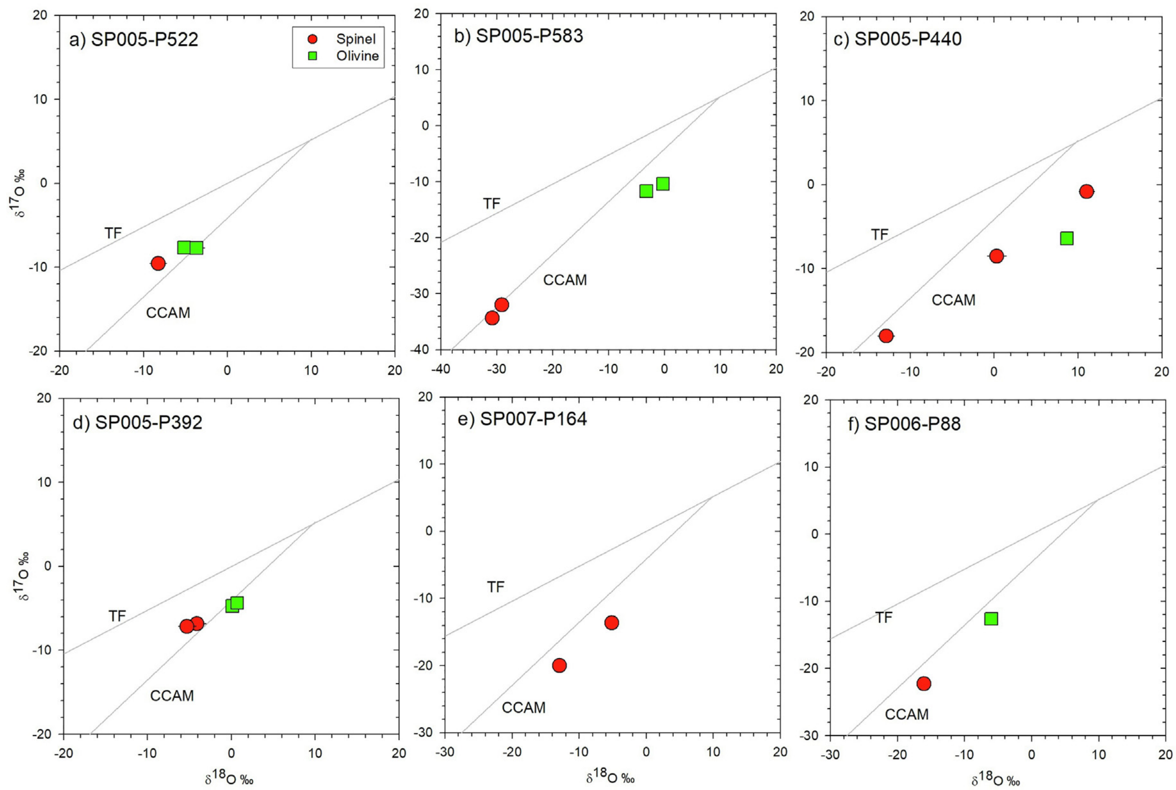

Fig. 5. The Oxygen three-isotope ratios of spinel-bearing MMs (A) SP005-P522, (B) SP005-P583, (C) SP005-P440, (D) SP005-P392, (E) SP005-P164, and (F) SP005-P88. The red circles denote spinel minerals, which are ^{16}O-enriched relative to their corresponding olivine grains (denoted by green squares). O-isotope data used in this plot is provided in Table 2. Except for SP005-P440 (C), most of the data plot close to CCAM line. The TFL is shown for reference.

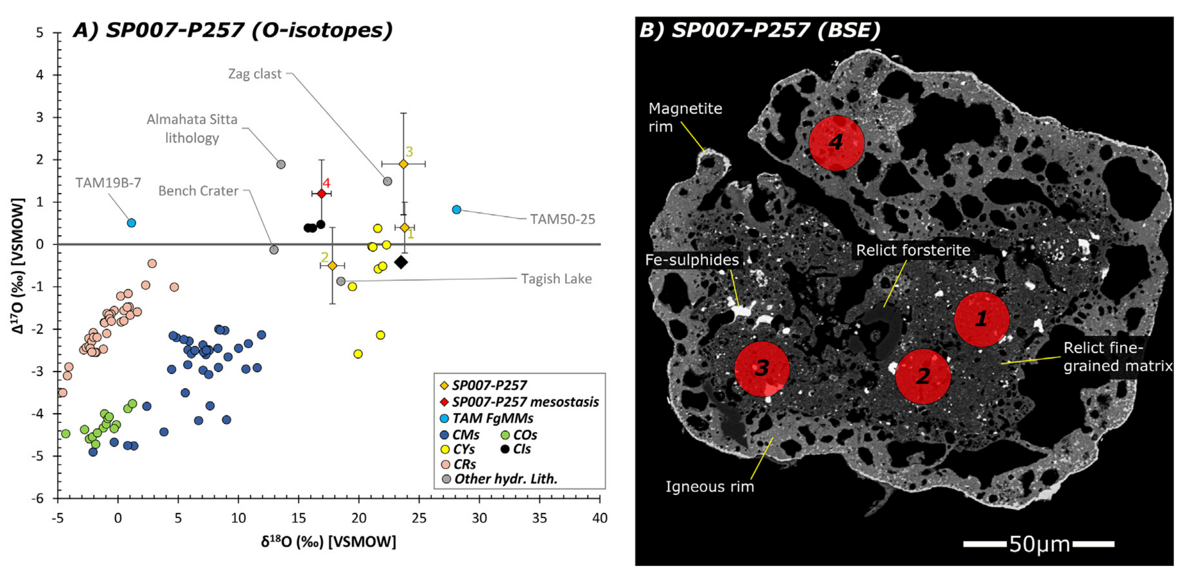

Fig. 6. Combined (A) O-isotope and (B) BSE image data from the scoriaceous FgMM SP007-P257. (A) O-isotope data are plotted in $\delta^{18}O$–$\Delta^{17}O$ isotope space alongside reference data from other hydrated CC materials. The four spot analyses collected on this MM have a ^{16}O-poor composition that spans a wide compositional range. This range partially overlaps with the fields of the CI and CY chondrites as well as the CI-like clast reported in the Zag meteorite. The approximate locations of the four O-isotope analyses are marked on the BSE image and indicated in (A) by coloured digits. Reference data were obtained from: Clayton and Mayeda, 1999; Ivanova et al., 2010; Schrader et al. 2011, 2014; Goodrich et al., 2019; Kebukawa et al., 2019; Kimura et al., 2020; Joy et al., 2020; Suttle et al., 2020.

sterite analyses plot close to the intersection of the slope-1 lines with the TFL. After considering the maximum 2σ variation in measurement uncertainties, 10 analyses have $\Delta^{17}O$ values > 0‰ (i.e. above the TFL), while 52 analyses have $\Delta^{17}O$ values < 0‰ (i.e. below the TFL). The remaining nine analyses are within error of the TFL and thus have compositions statistically indistinguishable from a $\Delta^{17}O = 0$‰ value.

By comparison, the O-isotope compositions of 11 spinel grains occupy a larger spread in $\delta^{18}O$–$\delta^{17}O$ isotope space. Their $\delta^{17}O$ values vary between −34.4‰ and −0.9‰, $\delta^{18}O$ values vary between −30.8‰ and +11.0‰ and $\Delta^{17}O$ values vary between −18.3‰ and −4.4‰ (Figs. 4 and 5). All spinel grains thus have compositions that fall below the TFL and, in many instances their compositions are significantly more ^{16}O-rich than the olivine grains studied here (Fig. 5). This relationship is best demonstrated in MMs where both spinel and forsterite are present (Fig. 5). In almost every instance spinel grains have isotopically lighter ^{16}O-enriched compositions than their corresponding olivine grains. Interestingly, however, we also note that, while most spinel grains show minimal isotopic variation, analyses on three spinel grains in the PO cosmic spherule SP005-P440 (Fig. 5c) cover a wide

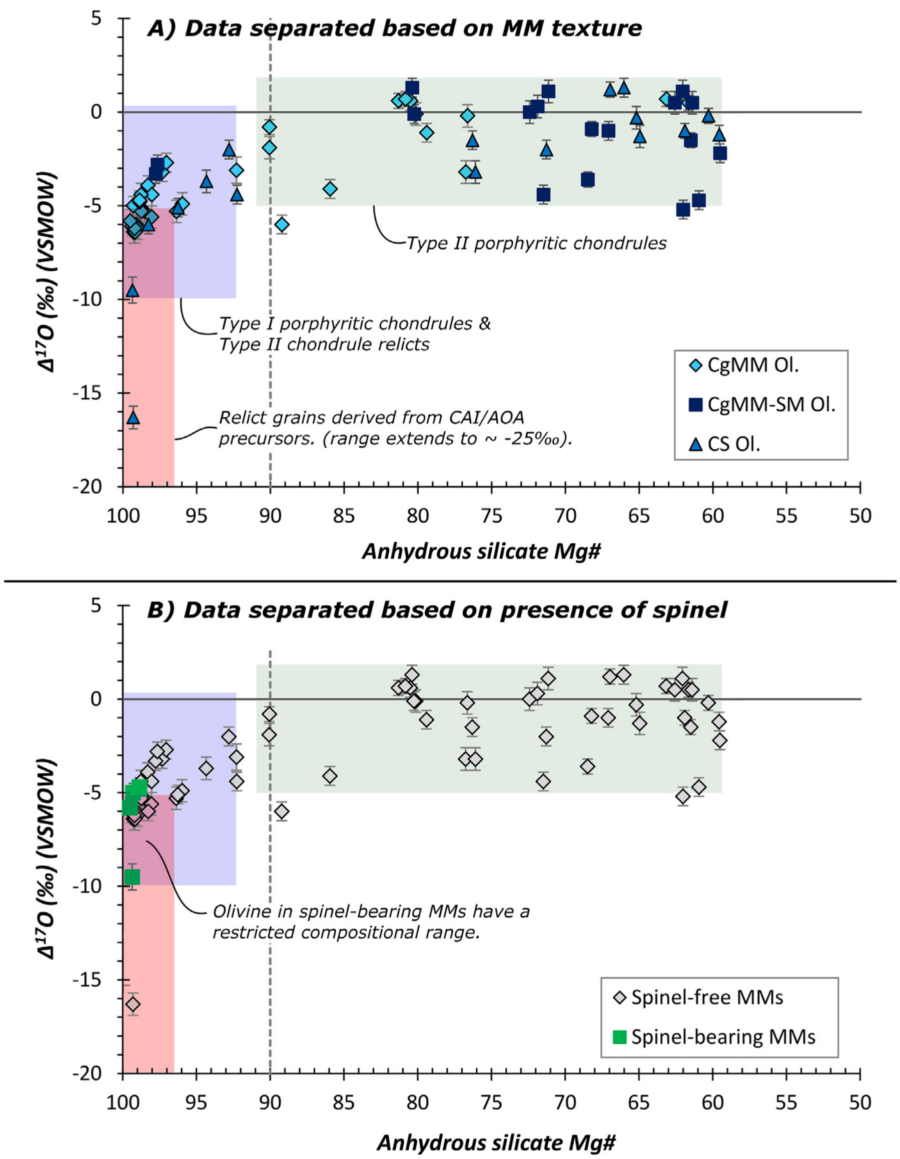

Fig. 7. Combined chemical (Mg#) and O-isotope ($\Delta^{17}O$) data for the 71 anhydrous silicates analysed in this study. Data is separated based on MM texture (A) or based on the presence/absence of (Mg-Al) spinel grains (B). There is no clear correlation based on MM texture. By contrast, spinel-bearing MMs always have high-Mg compositions and $\Delta^{17}O$ values between −10‰ and −4‰. These spinel-bearing particles most likely sample CAI/AOA material, while the spinel-free MMs most likely sample chondrules (or matrix-hosted silicates). Assuming this is correct, a grain's Mg#/$\Delta^{17}O$ values can be used to infer whether it is a sample of a type I or type II chondrule. Both types are represented among the study population.

O-isotope range, with one of the spinel analyses ($\Delta^{17}O$ = −6.6‰) having a more ^{16}O-poor composition than the MM's mesostasis ($\Delta^{17}O$ = −10.9‰).

We collected ten analyses on mesostasis regions within MMs. Seven were from cosmic spherules that had $\delta^{17}O$ values vary between −11.7‰ and +15.1‰, $\delta^{18}O$ values vary between −3.6‰ and +30.9‰ and $\Delta^{17}O$ values between −10.9‰ and +1.2‰ (Fig. 4). Only two analyses plot along the slope-1 reference lines, while five have values closely associated with these slope-1 lines but are located slightly below the CCAM – shifted to heavier ^{16}O-poor compositions. The remaining three mesostasis analyses have distinct compositions with $\delta^{18}O$ values > 15‰ and $\Delta^{17}O$ values close 0‰.

We also obtained four analyses on single FgMM (SP007-P257, Fig. 6), collecting three analysis regions in the particle's relict fine-grained matrix and a single analysis within the particle's igneous rim (a mesostasis analysis). This MM has an unusually ^{16}O-poor composition with mean average values of $\delta^{17}O$: +11.9‰, $\delta^{18}O$: +21.8‰ and $\Delta^{17}O$: +0.6‰.

5.3. Correlation between chemical and oxygen isotopic compositions of minerals

In a Mg#-$\Delta^{17}O$ plot (Fig. 7A) olivine grains span the range defined by type I and type II chondrules. However, no overall trend is apparent based on MM classification (CgMM vs. CgMM-SM vs. PO cosmic spherules). By contrast, if spinel-bearing and spinel-free MMs are compared (Fig. 7B) it can be seen that in spinel-bearing MMs forsterite grains always have a highly restricted compositional range in both chemistry and O-isotopes. Anhydrous silicate grains in spinel-free MMs (n = 66) vary in Mg# between 59.5–99.5 with all but one analysis plotting within the $\Delta^{17}O$ range: −7‰ to +2‰. By contrast, in spinel-bearing MMs anhydrous silicates (n = 5) were exclusively forsterites with distinctly Mg-rich compositions (Fo > 98.5) and a $\Delta^{17}O$ range of: −10‰ to −4‰ (Fig. 7B). Another notable feature is the observation that all anhydrous silicates with $\Delta^{17}O$ values > 0‰ have Mg#<85.

We compared the Cr abundance (Cr_2O_3 wt.%) against O-isotope composition ($\Delta^{17}O$ values) for the 11 spinel grains analysed (Fig. 8). They separate into two distinct groups: a low $\Delta^{17}O$ (<−8‰)/low Cr_2O_3 (<0.5 wt.%) group and a high $\Delta^{17}O$ (>−8‰)/high Cr_2O_3 (>1.0 wt.%) group.

6. DISCUSSION

6.1. Effects of atmospheric entry heating

Previous studies have investigated the bulk O-isotope composition of MMs. As a result, the modification of a particle's pre-atmospheric O-isotope composition is well-studied both for melted cosmic spherules (Yada et al., 2005; Suavet et al., 2010; Cordier and Folco, 2014; Van Ginneken et al., 2017; Goderis et al., 2020; Rudraswami et al., 2020b) and unmelted/scoriaceous particles (Suttle et al., 2020). Two effects operate: (i) mass-dependent fractionation, arising due to the preferential evaporation of light oxygen (^{16}O) shifts a particle's bulk composition to isotopically heavier values and (ii) O-isotope exchange with terrestrial oxygen present within the stratosphere (whose value is conventionally given as: $\delta^{17}O$: +11.8‰, $\delta^{18}O$: +23.5‰, $\Delta^{17}O$: −0.42‰ [Thiemens et al., 1995]) results in the progressive equilibration of the particle's bulk composition with that of the stratospheric composition. Suavet et al. (2010) suggested that mass-dependent fractionation and isotopic exchange with terrestrial oxygen contribute approximately equally. However, more recent work, analysing a larger population of cosmic spherules (n = 137) observed a statistically robust correlation between a MM's $\delta^{18}O$ composition and its peak temperature (as inferred from cosmic spherule quench textures) (Rudraswami et al., 2020b). This strongly suggests that mass-dependent fractionation dominates over mixing with stratospheric oxygen, even once particles achieve a molten state.

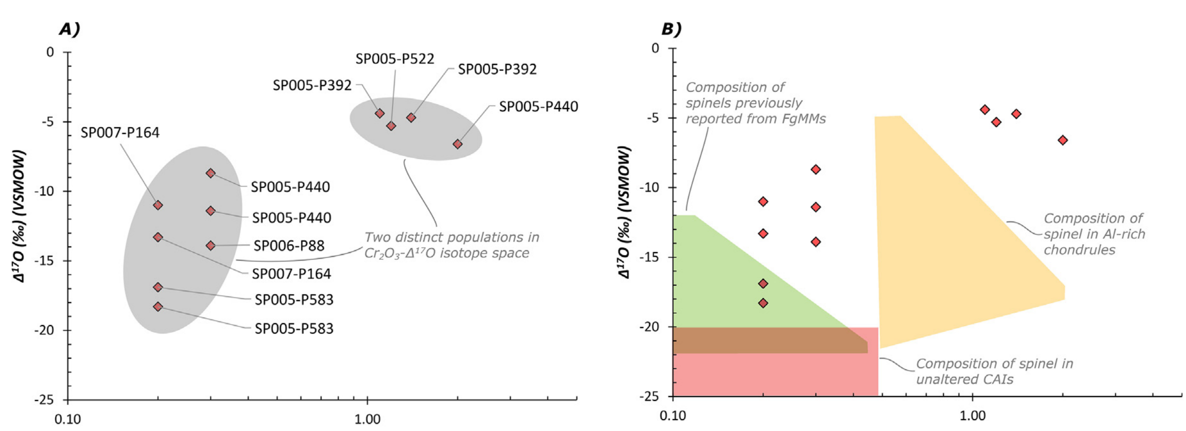

Fig. 8. (A) The chemical (Cr_2O_3 abundance [wt.%]) and O-isotope composition ($\Delta^{17}O$ [‰]) of the 11 Mg-Al spinel grains analysed. Spinel analyses separate into two distinct populations. (B) Interpretation of the reported spinel composition by comparison against previously reported data. Fields for pristine CAIs, spinels in Al-rich chondrules (Zhang et al., 2020b) and spinels in aqueously altered FgMMs (Kurat et al., 1994a; Hoppe et al., 1995; Engrand et al., 1999) are shown.

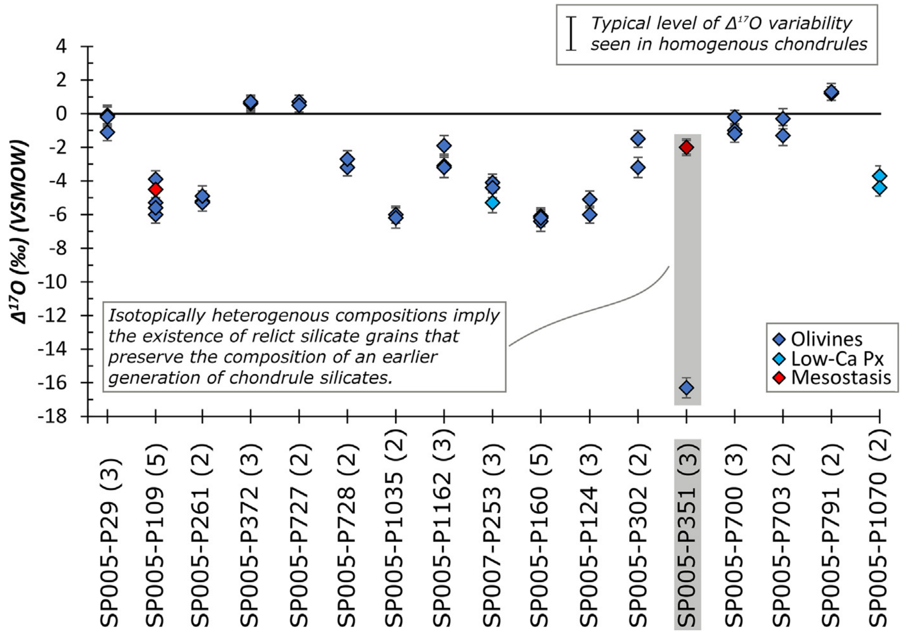

Fig. 9. Investigating $\Delta^{17}O$ variability in selected MMs. Assuming spinel-free CgMMs and RGB PO cosmic spherules are samples of chondrules, variability in a sample's $\Delta^{17}O$ provides an indication of whether that chondrule was either isotopically homogenous or heterogenous (denoted by grey shading). Most chondrules are isotopically homogenous ($\Delta^{17}O$ variability < 2‰). Heterogeneity implies the presence of relict silicates derived from an earlier generations of chondrule crystallization. This may be either a previous chondrule silicates (not seen here) or in rare cases a silicate grain derived from a CAI/AOA precursor (as in the case of SP005-351, identified based on its ^{16}O-rich signature [$\Delta^{17}O < -10$‰]). Note, only spinel-free MMs with grain cluster textures and which have more than one data point are shown. Thus, CgMM-SM particles and CgMMs with only one spot analysis have been omitted since isotopic heterogeneity cannot be investigated in these particles due to either insufficient data or insufficient mineral grains.

Thus, even in the most extreme scenario where a MM experiences high peak temperatures, long duration heating and significant alteration of its original $\delta^{17,18}O$ values the particle will still retain the approximate $\Delta^{17}O$ value of its precursor. This is because mass-dependent fractionation shifts the particle's composition to heavier values along a 0.52 slope line, leaving its $\Delta^{17}O$ value unaffected (Yada et al., 2005; Suavet et al., 2010, 2011; Rudraswami et al., 2015, 2016, 2020b). Furthermore, significant alteration of a sample's $\Delta^{17}O$ value (by mixing with stratospheric oxygen) is unlikely as this requires a change of ~ 10‰ in $\delta^{18}O$ to achieve a corresponding change of ~ 1‰ in $\Delta^{17}O$ (Rudraswami et al., 2015).

Finally, modifications to O-isotope signatures in relict grains will be even less extreme than those observed for bulk analyses because experimentally determined O-isotope diffusion rates in olivine grains are extremely low, even at high temperatures (~50% equilibration achieved between olivine and vapour when temperatures are held at the liquidus for ~ 5 min [Yu et al., 1995]). This knowledge combined with the observation that MMs are typically heated for < 10 s provides little opportunity for isotopic exchange between a relict mineral grain and silicate melt or indeed with atmospheric air.

The O-isotope signatures measured from relict forsterite and spinel in the present study can therefore be confidently assigned to pre-atmospheric processes, while O-isotope values obtained from MM mesostasis will have been altered in $\delta^{17,18}O$, being shifted to higher $\delta^{18}O$ values but will retain the approximate $\Delta^{17}O$ composition of their parent body.

6.2. The parent body affinities of MMs

We split the studied MMs into four populations and discuss their petrographic and O-isotope data and inferred parent bodies separately: (i) spinel-free CgMMs and RGB PO cosmic spherules (Section 6.2.1), (ii) relict silicates in chondrules derived MMs (Section 6.2.2), (iii) spinel-bearing MMs (Section 6.2.3) and (iv) the FgMM (Section 6.2.4).

6.2.1. Spinel-free CgMMs & RGB PO cosmic spherules – samples of chondrules

We investigated 21 spinel-free CgMMs (including nine particles dominated by a single mineral [CgMM-SM]). The petrographic properties of these particles are consistent with refractory minerals found in chondritic meteorites. Among the CgMMs with a grain aggregate texture both their mineralogy and chemical compositions are indistinguishable from chondrules (or fragments thereof), being composed primarily of Mg-rich (Mg#>70) anhydrous silicates and containing minor Fe-Ni metal, Fe-sulphides and/or silicate glass. Meanwhile the CgMM-SMs varieties may represent a single mineral grain derived from a chondrule, or a matrix-hosted isolated anhydrous silicates (which have close relationships with chondrules; e.g., Jacquet et al., 2021). The O-isotope compositions of all our forsterite and pyroxene plot on, or close to the slope-1 reference lines and within the O-isotope range most commonly associated with chondrules (Fig. 4). As such both their chemical and isotopic properties support a link to matrix-hosted anhydrous silicates and chondrule-derived silicates. We also investigated eight spinel-free RGB cosmic spherules. However, both chemically and isotopically the forsterite grains in the cosmic spherules are compositionally indistinguishable from their corresponding phases found in the unmelted CgMMs studied here (Fig. 7A). This indicates that relict forsterite grains in both MM types (UMMs and cosmic spherules) can be treated together as a single population.

The relationship between mineral chemistry and O-isotope composition in chondrules can be evaluated using an Mg#-Δ^{17}O plot (Fig. 7). These plots provide insights into the conditions that existed in different chondrule-forming regions within the protoplanetary disk. Chondrules from the inner solar system (e.g. Scott et al., 2018) non-carbonaceous chondrite (NC) meteorites (the Ordinary, Enstatite, Kakangari and Rumuruti groups) show no relationship between Mg# and Δ^{17}O composition (Kita et al., 2010; Weisberg et al., 2011; Nagashima et al., 2015; Miller et al. 2017). By contrast, chondrules from outer solar system CCs demonstrate a correlation between Mg# and Δ^{17}O. Reduced high-Mg type I chondrules (Mg#>90) generally have ^{16}O-rich compositions (with Δ^{17}O between −10‰ and 0‰ and averaging ∼ −5‰), while oxidized low-Mg type II chondrules (Mg#<90) generally have ^{16}O-poor compositions (Δ^{17}O ∼ −2‰) (Ushikubo et al., 2012; Tenner et al., 2013, 2015, 2018; Chaumard et al., 2018; Hertwig et al., 2018; Ushikubo and Kimura, 2021). The formation of isotopically heavy type II chondrules are interpreted as evidence of extreme dust enrichment (Tenner et al., 2015; Hertwig et al., 2018) or interaction between the chondrule-forming reservoir and either a ^{16}O-poor gas phase (Schrader et al., 2013) or the accretion of ^{16}O-poor water-ice onto chondrules prior to remelting (e.g. Schrader et al., 2013; Hertwig et al., 2018; Chaumard et al., 2018). Furthermore, multiple high-precision studies have collectively demonstrated that different subgroups of CC show subtle variations in their Mg#-Δ^{17}O distribution (see Fig. 4 in Ushikubo and Kimura [2021] as an example). Most notably type II chondrules with Δ^{17}O > 0‰ (and up to Δ^{17}O: +2‰) are found in the CR chondrites (Schrader et al., 2013; Tenner et al., 2015), in Tagish Lake (TL) (Ushikubo and Kimura, 2021), the TL-like meteorites WIS 91600 and MET 00432 (Yamanobe et al., 2018) and in the WILD2 silicates (Nakashima et al., 2012; Joswiak et al., 2014; Defouilloy et al., 2017). These ^{16}O-poor (Δ^{17}O > 0‰) chondrules are associated only with outer solar system D-type asteroids

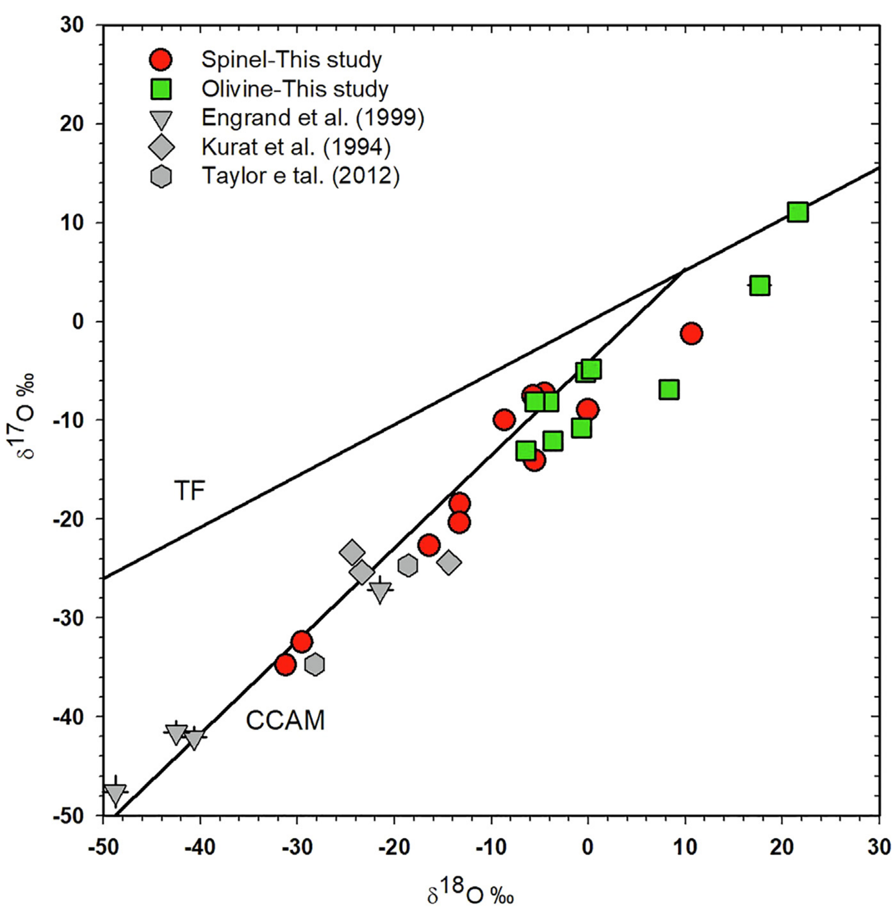

Fig. 10. Oxygen isotope data from spinel minerals in spinel-bearing MMs. Plot includes data from this study along with literature data (Kurat et al., 1994a; Engrand et al., 1999; Taylor et al., 2012). Errors reported are 2σ. The TFL and CCAM line are shown for reference. Some of the analyses on SP005-P583 and SP005-P164 from this study were made on the same grains as Taylor et al. (2012).

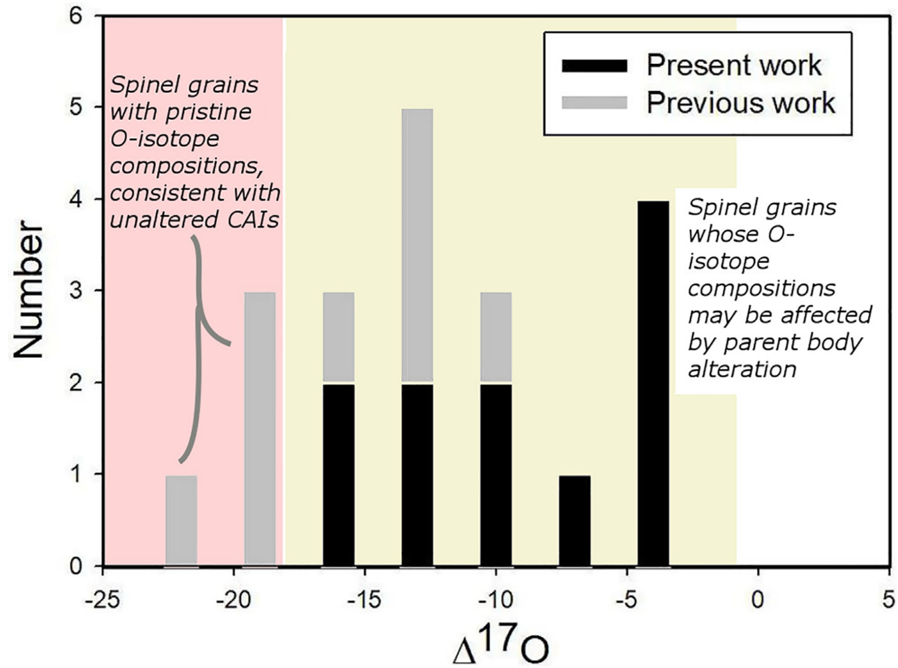

Fig. 11. The histogram plot of $\Delta^{17}O$ compositions of spinel grains in spinel-bearing MMs from the present study and from the literature (Kurat et al., 1994a; Engrand et al., 1999; Taylor et al., 2012). Our study has effectively doubled the number of spinel grains analysed within a MM host. Note, $\Delta^{17}O \leq -20‰$ are consistent with pristine CAIs, while ^{16}O-depleted compositions ($\Delta^{17}O > -20‰$) indicate reprocessed CAIs affected either by nebula processes (i.e. O-isotope exchange with nebula gas or silicate melts) or affected by parent body processing (i.e. thermal or aqueous alteration).

and cometary materials and therefore appear to have been produced at large heliocentric distances.

Micrometeorites sample a range of dust-produced small bodies. However, by comparing the Mg#-$\Delta^{17}O$ distribution of our spinel-free MMs (Fig. 7), which represent chondrule fragments against equivalent data from various chondrite groups (Fig. 4 in Ushikubo and Kimura, 2021) we can evaluate which parent bodies these MMs are sampling. Our MM population shows minimal overlap with the ranges measured for OC chondrules, which generally have Mg#>70 and $\Delta^{17}O > -0.5‰$. Instead, over the type I chondrule range (Mg#>90) our MM population most closely matches the spread defined by CO, CM and Acfer 094 chondrules ($\Delta^{17}O < -2‰$ and with a slight positive correlation [Ushikubo et al., 2012; Tenner et al., 2013; Chaumard et al., 2018]). Meanwhile, over the type II chondrule range (Mg#<90) our MM population includes a large variation in $\Delta^{17}O$ ($-5‰$ to $+2‰$) which is generally inconsistent with a CO-CM range and is instead similar to the CR chondrites, TL and the TL-like meteorites and cometary silicates. Thus, although we cannot assign any individual MM to a specific chondrite group this technique allows an estimation of the provenance of the population as a whole. Nevertheless, OC precursors are relatively abundant amongst the coarse size fractions of MMs with sizes > 300 μm, many studies support the concept that the smaller size MMs are overwhelmingly dominated by CC precursor, our work also support this observation. We conclude that these spinel-free MMs are chondrule fragments from CC chondrules. They most likely sample a mix of CM and either CR, TL-like or cometary materials.

6.2.2. Relict silicates in chondrule-derived MMs

Rare ^{16}O-rich olivine grains are found within otherwise isotopically homogenous ($\Delta^{17}O < 2‰$) porphyritic chondrules in both CC and OC meteorites (Jones et al., 2004; Krot et al., 2006; Kita et al., 2010; Ushikubo et al., 2012; Marrocchi et al., 2018b, 2019; Schneider et al., 2020). They are interpreted as relict minerals which survived (potentially multiple) transient melting and recrystallization events during chondrule formation (Jones, 1996). Depending on the magnitude of their ^{16}O-enrichment they could be derived from either an earlier generation of chondrule (e.g., Type I grains held within a Type II chondrule; Ruzicka et al., 2008) or from a more refractory CAI/AOA source (Jones et al., 2004; Marrocchi et al., 2019).

In this study we identified a single MM – SP005-P351 (Fig. 1a) hosting a forsterite grain with a distinctly ^{16}O-rich composition ($\delta^{17}O$: $-28.2‰$, $\delta^{18}O$: $-22.8‰$ and $\Delta^{17}O$: $-16.3‰$; Fig. 4, Fig. 9). This composition is within the range reported form CAIs and AOAs (Tenner et al., 2018). The other forsterite grain analysed in this particle had an O-isotope composition ($\delta^{17}O$: $+0.2‰$, $\delta^{18}O$: $+4.3‰$ and $\Delta^{17}O$: $-2.0‰$), consistent with chondrule olivine found in CCs. Particle SP005-P351 is therefore best interpreted as a type I chondrule fragment from a CC precursor which contains a single relict olivine grain originating from a refractory inclusion. The relict silicate was most likely derived from an AOA (rather than a CAI) because olivine is common in these inclusions (and rare in CAIs).

Isotopically light relict chondrule silicates often have Mg-rich compositions (Mg#>90 [Fa < 10]) (Hervig and

Steele, 1992; Leshin et al., 1997; Hiyagon and Hashimoto, 1999; Ushikubo et al., 2012; Tenner et al., 2013, 2015). However, olivine grains with high Fa contents and low $\Delta^{17}O$ values (^{16}O enrichment) have also been identified (Jones et al., 2004; Ushikubo et al., 2012). These Fe-rich relict olivines may have originally started out as Mg-rich varieties but experienced advanced Mg-Fe equilibration with their host chondrule melt, whilst also retaining their initial ^{16}O-rich signature. This is possible because solid-state diffusion rates for Mg-Fe cations are orders of magnitude faster than the diffusion rates of O-isotopes (Dohmen et al., 2007; Chakraborty, 2010). As a result, although the identification of the relict ^{16}O-rich grain in SP005-P351 was relatively straightforward (both due to its high-Mg chemistry and extremely light $\Delta^{17}O$ values), this is not always the case. Some of the other olivine grains with less extreme compositional variation may also be relict silicates from earlier generations of chondrules. Since the O-isotope compositions of relict grains often fall within the same range as the chondrules (namely between −6‰ and −2‰; e.g., Rudraswami et al., 2011; Tenner et al., 2018) and chemical composition cannot be used as a reliable indication. The only way to confidently identify additional relict grains is to collect multiple silicate analyses on different grains within a single chondrule (or in this case chondrule-like MM) and determine if the O-isotope range is either homogenous ($\Delta^{17}O < 2‰$) or heterogeneous ($\Delta^{17}O > 2‰$), with heterogeneous compositions implying the existence of relict grains. Using this criterion (Fig. 9) we demonstrate that no other MM appears to contain relict grains, since all other particles have O-isotope variability $\Delta^{17}O \leq 2‰$ (Fig. 9).

6.2.3. ***Spinel-bearing MMs** – samples of CAIs and Al-rich chondrules*

There are three types of spinel found in chondritic materials: (i) primary spinels formed in the nebula, prior to the accretion of chondrites; (ii) secondary spinels formed on the parent asteroid by precipitation from fluids and (iii) spinels formed during atmospheric entry by oxidation and crystallization of a chondritic melt. Primary spinel grains have predominantly Mg-Al compositions (MacPherson et al. 1988; Zhang et al. 2020a), while secondary spinels have Cr- and Fe-rich compositions (Tomeoka and Buseck, 1985; Grossman and Brearley, 2005; Zolotov, 2012) and spinels formed during atmospheric entry appear as Ni-bearing magnetite and are located exclusively in the mesostasis of unmelted MMs or as magnetite grains in the fusion crusts in larger meteorites (Genge and Grady, 1999; Toppani et al. 2001). All the spinels analysed in this study have Mg-Al chemistries and primitive, ^{16}O-rich compositions. They are therefore interpreted as primary spinels.

Primary Mg-Al spinel grains are highly refractory minerals. They formed either as condensates of nebular gas composition at temperature below 1500 °C (Lodders, 2003) or during crystallization of Al-rich chondrule melts (Krot and Keil, 2002; MacPherson and Huss, 2005; Tronche et al., 2007; Krot et al., 2009). Spinels in CAIs were likely some of the earliest minerals to form in the solar nebula (Lodders, 2003; Krot et al., 2009). Conversely, their presence in chondrules is interpreted as evidence of CAI material being transported into chondrule-forming regions and becoming consumed as chondrules experienced multiple episodes of melting, crystallization and interaction with the surrounding nebula gas and dust (Maruyama et al., 1999; Krot and Keil, 2002; MacPherson and Huss, 2005).

The O-isotope compositions of Mg-Al spinels in chondrites plot on, or close to the slope-1 reference lines and fall within the isotopic range ($\Delta^{17}O$: −25‰ to −2‰ [Fig. 7 in Krot et al., 2009; Zhang et al., 2020a]). Isotopically light values ($\Delta^{17}O \leq -20‰$) are consistent with pristine unaltered CAIs, while those affected by asteroidal alteration have compositions in the range:

$-20‰ < \Delta^{17}O < +2‰$ (Itoh et al., 2004; Krot et al., 2009, 2019; Zhang et al., 2020a). Additionally, isotopically light compositions ($\Delta^{17}O \leq -20‰$) were produced where CAI-derived spinels were incorporated into (Al-rich) chondrules (Krot et al., 2009; Zhang et al., 2020b). These grains would have been subject to high-temperature partial melting during chondrule heating events, leading to incomplete O-isotope exchange between the spinel grain and their host chondrule melt and/or with the surrounding nebula gas. Such reactions produced heavier ^{16}O-poor compositions (relative to pristine CAIs), with $\Delta^{17}O$ values between −20‰ and −5‰ being characteristic (Maruyama et al., 1999; Russell et al., 2000; Krot et al., 2009, 2019; Zhang et al., 2020b).

Micrometeorites containing Mg-Al spinel grains are very rare (≪1%; Genge et al., 2008; Taylor et al., 2012). We analysed seven spinel-bearing MMs (two were previously analysed by Taylor et al. (2012) – SP005-P583 and SP007-P164), collecting 11 independent analyses on separate spinel grains (Figs. 8, 10 and 11). For a single particle (SP006-P102) the target spinel grain was too small to analyse, so only the surrounding MM mesostasis was investigated isotopically. Our measured spinels plot on, or close to the slope-1 reference lines (except few which are slightly deviated from this trend [Figs. 4 and 10]) and vary from $\Delta^{17}O$: −18.3‰ to −4.4‰. Several Mg-Al spinel-bearing MMs with associated O-isotope data (Figs. 10 and 11) have been published previously. Kurat et al. (1994a) and Hoppe et al. (1995) reported data for three spinel-bearing MMs (with particle IDs: MM92/15-23, MM94-1 #28 and MM94-4 #36), they were FgMMs containing (dehydrated) Fe-rich phyllosilicate and hosting small Mg-Al spinels with O-isotope compositions in the range: $-19.2‰ \leq \Delta^{17}O \leq -10.5‰$. Later, Engrand et al. (1999) reported two spinel-bearing FgMMs (92-13C-23 and 94-4b-5), whose spinels had $\Delta^{17}O$ compositions of −20.7‰ and −15.8‰ respectively. The particle with the isotopically lightest spinel grain (92-13C-23) also contained a small quantity of melilite (a mineral found exclusively in pristine and minimally altered CAIs). Most recently Taylor et al. (2012) reported 50 μm spinels in two spinel-bearing cosmic spherules with spinel compositions of $\Delta^{17}O$: −19.8‰ and $\Delta^{17}O$: −14.8‰, respectively. However, one of the MM SP005-P440 has oxygen isotope data deviated to right side of slope-1 line, while the other spinel particles are closer to CCAM line (Fig. 5c) indicating that spinel in this particle had undergone thermal processing such as evaporation, melting and recrystallization analogous to fractionation and unidentified nuclear isotope anomalies (FUN) CAIs that follow trends parallel to the TFL (Thrane et al., 2008). This suggests the precursor of this CAI experienced isotopic exchange with nebular gas, thereby altering its original isotopic compositions (Thrane et al., 2008; Makide et al., 2009).

All the Mg-Al spinels grains reported from MMs to date (both in the literature and in this study) have ^{16}O-depleted ($\Delta^{17}O > -20‰$) compositions (Fig. 8B), outside the range reported for pristine CAIs. In Fig. 8A we demonstrated that two populations of spinels exist a low Cr_2O_3 group and a high Cr_2O_3 group. The low-Cr population are likely CAI-derived spinels that have been affected by parent body aqueous alteration. This interpretation is based on two factors: (i) low-Cr contents ($Cr_2O_3 \leq 0.5$ wt.%) are typical of CAI-derived spinels (as opposed to the spinels found in Al-rich chondrules, which are otherwise Cr-enriched [Maruyama and Yurimoto, 2003; Rudraswami et al., 2011]). Furthermore (ii) most previously reported low-Cr spinels are found in hydrated FgMMs. Surrounding particle textures therefore offer context. Among the literature several spinels in hydrated FgMMs are reported. Here Fe-rich phyllosilicates (or their thermal decomposition products) are observed mantling the Mg-Al spinel phase. They therefore experienced an episode of protracted parent body aqueous alteration which could have affected spinel grain's isotopic composition, similar to those reported by Zhang et al. (2020b) from CO chondrites.

By contrast, spinel grains with high-Cr contents most likely originate from an Al-rich chondrule precursors. In both SP005-P522 and SP005-P392 their spinel grains are enclosed by magnesian olivine crystals and have $\Delta^{17}O$ values that fall within the typical range of type I chondrules from CCs. Furthermore, elevated Cr abundances (Cr_2O_3-≥ 0.5 wt.%) in spinels are characteristic of Al-rich chondrules (Maruyama and Yurimoto, 2003; Rudraswami et al., 2011). Finally, we note that the origin of spinels in SP005-P440 are less clear. This particle contains three spinels with variable Cr contents (Cr_2O_3: 0.3, 0.3 and 2.0 wt.%, Fig. 8) and O-isotope compositions mass fractionated off the slope-1 reference lines (Fig. 5c).

6.2.4. The FgMM SP007-P257

Particle SP007-P257 is dominated by a dark Mg-rich matrix and contains small Fe-sulphides and anhedral anhydrous silicate grains. Inside the igneous rim Fe-sulphides occur as rounded beads that abut vesicles. These textures attest to sulphide decomposition at temperatures between 800 and 1100 °C (Greshake et al., 1998; Taylor et al., 2011). The particle's matrix also shows evidence of phyllosilicate dehydration cracks although a vesicular texture dominates. During atmospheric entry phyllosilicates dehydrate at relatively low temperatures (~350–800 °C) and subsequently recrystallize to form a groundmass of nanocrystalline olivine (Suttle et al., 2017). As heating advances the formation of vesicular matrix is associated with peak temperatures > 1200 °C (Toppani et al., 2001; Taylor et al., 2011). Thus, although the relict matrix inside this MM did not melt, it experienced significant thermal reprocessing. This MM's mineralogy and texture are typical of scoriaceous FgMMs.

Previous research has demonstrated a clear link between FgMMs and hydrated CC materials (Kurat et al., 1994b; Engrand and Maurette, 1998; Genge et al., 1997; Taylor et al., 2012; Badyukov et al., 2018; Suttle et al., 2019, 2020b). It is therefore reasonable to assume that SP007-P257 derives from a hydrated CC precursor and as such we have compared its O-isotope composition against a wide range of hydrated CC precursors (Fig. 6A).

Three spot analyses were collected within the relict fine-grained matrix of particle SP007-P257 (Fig. 6B), they have ^{16}O-poor compositions characterized by $\delta^{17}O$: +8.8‰ to +14.2‰, $\delta^{18}O$: +17.8‰ to +23.8‰ and $\Delta^{17}O$: −0.5‰ to +1.9‰. The single mesostasis analysis, collected within the sample's igneous rim revealed a composition of $\delta^{17}O$: +10.0‰, $\delta^{18}O$: +16.9‰ and $\Delta^{17}O$: +1.2‰. Atmospheric entry heating will have mass-fractionated the composition of SP007-P257 towards higher $\delta^{18}O$ values, although interestingly the mesostasis analysis exhibits the lowest $\delta^{18}O$ composition, implying that mass-dependent fractionation has not significantly affected this MM's composition and also that the sample's pre-atmospheric O-isotope composition was characterised by high $\delta^{18}O$ values (> +15‰).

The four analyses on SP007-P257 span a wide compositional range that partially overlaps with the fields of the CI chondrites and the newly defined CY chondrites (King et al., 2019) as well as the composition of Tagish Lake and the composition of an organic-rich clast held within the Zag meteorite (Kebukawa et al., 2019). Particle SP007-P257 may therefore be related to one of these parent bodies or sample a different object that has a similar O-isotope composition. However, based on the MM's petrography this sample is unlikely to be directly related to any of these lithologies (for example SP007-P257 lacks sufficient sulphides to be related to the CYs, contains anhydrous silicates which are very rarely found in CIs and lacks both organics and carbonates which are common components of the Zag xenolith and the Tagish Lake meteorite respectively [though their absence may be a result of atmospheric entry heating]).

In recent years there has been a significant increase in the number of reported hydrated CC lithologies whose O-isotope compositions plot on or above the TFL ($\Delta^{17}O$: $\geq$0‰) and have $\delta^{18}O$ values > +10‰ (King et al., 2019; Goodrich et al., 2019; Kebukawa et al., 2019; Suttle et al., 2020). They represent a diverse set of water-rich C-type asteroids whose heavy bulk O-isotope compositions appear to be related to either the accretion of abundant ^{16}O-poor water (Chaumard et al., 2018; Suttle et al., 2020; Marrocchi et al., 2018a) and/or affected by parent body thermal metamorphism (Ivanova et al., 2013; King et al., 2019). Data from SP007-P257 adds to this growing inventory as another sample of ungrouped water-rich isotopically heavy C-type asteroid.

7. IMPLICATIONS

Previous studies of unmelted CgMMs show that many of these particles are chondrules or fragments of chondrules (Engrand et al., 1999; Genge et al., 2005; Genge, 2008; Van Ginneken et al., 2012; Prasad et al., 2018; Dionnet et al., 2020; Rudraswami et al., 2020a) or in rare instances CAIs and AOAs (Kurat et al., 1994a; Hoppe et al., 1995; Greshake et al., 1996; Taylor et al., 2012). In addition, a small fraction of CgMMs, those containing olivine/pyroxene grains with both high-Mg (Mg#>98) and high-Mn (MnO $\geq$ 0.5wt.%) compositions may sample extremely refractory mineral aggregates similar to those reported from the comet 81P/WILD2 (Imae et al., 2013; Noguchi et al., 2015).

We identified material from both chondrules (spinel-free MMs dominated by Mg-rich olivine and whose O-isotope compositions plot on the slope-1 reference lines between Δ^{17}O: −6‰ and +4‰) and CAIs/AOAs (Mg-Al spinel-bearing MMs with or without olivine whose spinel grain compositions plot on the slope-1 reference lines with Δ^{17}O values < −4‰). Although our results support the conclusions of numerous previous in-situ O-isotope studies on forsterite grains in MMs (Engrand et al., 1999; Gounelle et al., 2005; Matrajt et al., 2006; Rudraswami et al., 2015) – namely that most small CgMMs are fragments of chondrules, primarily from CC parent bodies – we have also extended interpretations beyond this well-established paradigm by identifying both type I and type II chondrule varieties and through the recognition of a relict silicate grain with a ^{16}O-rich composition that suggests it was derived from an AOA precursor.

Analysis of MMs containing Mg-Al spinels also supports earlier work (Kurat et al., 1994a; Hoppe et al., 1995; Greshake et al., 1996; Taylor et al., 2012) which concluded these MMs sample CAI material. Building upon these inferences we note that most CAI-derived spinel grains show O-isotope evidence of partial exchange with a ^{16}O-poor reservoir and are therefore not pristine CAI material. Furthermore, spinel grains with the heaviest O-isotope compositions (Δ^{17}O > −8‰) also exhibit minor element Cr enrichment (Cr > 0.2 wt.%) suggesting interaction with parent body fluids. We conclude that most Mg-Al spinel grains are fragments of aqueously altered CAIs and derived from hydrated C-type asteroids.

8. CONCLUSIONS

Olivine is the dominant mineral in all types of MMs, while Mg-Al spinel grains are relatively rare. Their high melting points mean that forsterite and spinel grains frequently survive atmospheric entry without melting or significant sub-solidus alteration, ensuring that their pre-atmospheric chemical and O-isotope signatures are preserved. Except for mesostasis phases, data in the present study has not experienced significant alteration due to atmospheric entry. Our main conclusions are:

1. The diversity in O-isotope compositions measured here showcase the heterogeneity in solar system materials. Compositions reported from small MMs (<200 μm) parallel the range observed from primitive chondrites.
2. Spinel-free CgMMs (and RGB PO cosmic spherules) have clear chemical, textural and O-isotope links to chondrules. They appear to be sampling a mix of CM-like and either CR-like, Tagish Lake-like or cometary materials.
3. In chondrule-like MMs relict grains representing earlier generations of chondrule silicates can be identified by analysing multiple olivine grains in the same sample and testing for isotopic heterogeneity (Δ^{17}O > 2‰). This technique identified a relict silicate derived from a CAI/AOA precursor.
4. Mg-Al Spinels in MMs are very rare ($\ll$1% of MMs). Based on their ^{16}O-depleted compositions none of the grains analysed here are unaltered CAI-derived spinels. Instead, spinels with high Cr_2O_3 contents (>0.5 wt.%) and ^{16}O-poor compositions (Δ^{17}O > −8‰) probably originate from Al-rich chondrules while spinels with low Cr_2O_3 (<0.5 wt.%) and modest ^{16}O-depletions (−20‰ < Δ^{17}O < −8‰) are interpreted as CAI-derived spinels affected by a later period of parent body aqueous alteration.

Declaration of Competing Interest

The authors declare that they have no known competing financial interests or personal relationships that could have appeared to influence the work reported in this paper.

ACKNOWLEDGEMENTS

This work is funded by ISRO-PRL PLANEX and PMN-MOES project. The collection of MMs from SPWW is funded by the National Science Foundation. We thank Vijay Khedekar, Areef Sardar, and Lionel G. Vacher for their assistance during electron microscopy. We thank Sasha Krot, A. Hertwig and T. Ushikubo for their suggestions that improved the quality of the manuscript. NGR also thanks CSIR for Raman Research Fellowship to carry out the research at CRNS-CRPG, Nancy, France. This is NIO's contribution No. 6898.

APPENDIX A. SUPPLEMENTARY DATA

Supplementary data to this article can be found online at https://doi.org/10.1016/j.gca.2022.03.015.

REFERENCES

Badyukov D. D., Brandstaetter F. and Topa D. (2018) Fine-grained scoriaceous and unmelted micrometeorites: sources and relationships with cosmic spherules. *Geochem. Int.* **56**, 1071–1083.

Beckerling W. and Bischoff A. (1995) Occurrence and composition of relict minerals in micrometeorites from Greenland and Antarctica—implications for their origins. *Planet. Space Sci.* **43**, 435–449.

Blanchard M. B. and Cunningham G. G. (1974) Artificial meteor ablation studies: olivine. *J. Geophys* **79**, 3973–3980.

Bodénan J.-D., Starkey N. A., Russell S. S., Wright I. P. and Franchi I. A. (2020) One of the earliest refractory inclusions and its implications for solar system history. *Geochim. Cosmochim. Acta* **286**, 214–226.

Bridges J. C., Franchi I. A., Sexton A. S. and Pillinger C. T. (1999) Mineralogical controls on the oxygen isotopic compositions of UOCs. *Geochim. Cosmochim. Acta* **63**, 945–951.

Brownlee D. E. (2001). In *Accretion of Extraterrestrial Matter Throughout Earth's History*. Kluwer/Plenum, New York, pp. 1–12.

Brownlee D. E., Bates B. and Schramm L. (1997) The elemental composition of stony cosmic spherules. *Meteorit. Planet. Sci.* **32**, 157–175.

Carrillo-Sánchez J. D., Plane J. M. C., Feng W., Nesvorný D. and Janches D. (2015) On the size and velocity distribution of cosmic dust particles entering the atmosphere. *Geophys. Res. Lett.* **42**, 6518–6525.

Chakraborty S. (2010) Diffusion coefficients in olivine, wadsleyite, and ringwoodite. In *Reviews in Mineralogy and Geochemistry* (eds. Y. Zhang and D. J. Cherniak). Mineralogical Society of America, Washington D.C., pp. 603–639.

Chaumard N., Defouilloy C. and Kita N. T. (2018) Oxygen isotope systematics of chondrules in the Murchison CM2 chondrite and implications for the CO-CM relationship. *Geochim. Cosmochim. Acta* **228**, 220–242.

Chaussidon M., Libourel G. and Krot A. N. (2008) Oxygen isotopic constraints on the origin of magnesian chondrules and on the gaseous reservoirs in the early solar system. *Geochim. Cosmochim. Acta* **72**, 1924–1938.

Clayton R. N. and Mayeda T. K. (1999) Oxygen isotope studies of carbonaceous chondrites. *Geochim. Cosmochim. Acta* **63**, 2089–2104.

Clayton R. N., Mayeda T. K., Goswami J. N. and Olsen E. J. (1991) Oxygen isotope studies of ordinary chondrites. *Geochim. Cosmochim. Acta* **55**, 2317–2337.

Clayton R. N., Onuma N., Grossman L. and Mayeda T. K. (1977) Distribution of pre-solar component in Allende and other carbonaceous chondrites. *Earth Planet. Sci. Lett.* **34**, 209–224.

Cordier C. and Folco L. (2014) Oxygen isotopes in cosmic spherules and the composition of the near Earth interplanetary dust complex. *Geochim. Cosmochim. Acta* **146**, 18–26.

Cordier C., Baecker B., Ott U., Folco L. and Trieloff M. (2018) A new type of oxidized and pre-irradiated micrometeorite. *Geochim. Cosmochim. Acta* **233**, 135–158.

Defouilloy C., Nakashima D., Joswiak D. J., Brownlee D. E., Tenner T. J. and Kita N. T. (2017) Origin of crystalline silicates from Comet 81P/Wild 2: Combined study on their oxygen isotopes and mineral chemistry. *Earth Planet. Sci. Lett.* **465**, 145–154.

Dionnet Z., Suttle M. D., Longobardo A., Rotundi A., Folco L., Della C. V. and King A. (2020) X-ray computed tomography: Morphological and porosity characterization of giant Antarctic micrometeorites. *Meteorit Planet Sci* **55**, 1581–1599.

Dobrică E., Ogliore R. C., Engrand C., Nagashima K. and Brearley A. J. (2019) Mineralogy and oxygen isotope systematics of magnetite grains and a magnetite-dolomite assemblage in hydrated fine-grained Antarctic micrometeorites. *Meteorit Planet Sci* **54**, 1973–1989.

Dohmen R., Becker H.-W. and Chakraborty S. (2007) Fe-Mg diffusion in olivine I: experimental determination between 700 and 1200 °C as a function of composition, crystal orientation and oxygen fugacity. *Phys. Chem. Minerals* **34**, 389–407.

Engrand C., McKeegan K. D. and Leshin L. A. (1999) Oxygen isotopic compositions of individual minerals in Antarctic micrometeorites: further links to carbonaceous chondrites. *Geochim. Cosmochim. Acta* **63**, 2623–2636.

Engrand C. and Maurette M. (1998) Carbonaceous micrometeorites from Antarctica. *Meteorit Planet Sci* **33**, 565–580.

Folco L. and Cordier C. (2015) Micrometeorites. EMU Notes in Mineralogy. In *Planetary Mineralogy* (eds. M. R. Lee and H. Leroux), European Mineralogical Union. The Mineralogical Society of Great Britain and Ireland, pp. 253–297, Chap. 9, doi:10.1180/EMU-notes.15.9.

Genge M. J., Engrand C., Gounelle M. and Taylor S. (2008) The classification of micrometeorites. *Meteorit. Planet. Sci.* **43**, 497–515.

Genge M. J. (2006) Igneous rims on micrometeorites. *Geochim. Cosmochim. Acta* **70**, 2603–2621.

Genge M. J. (2008) Koronis asteroid dust within Antarctic ice. *Geology* **36**, 687–690.

Genge M. J., Gileski A. and Grady M. M. (2005) Chondrules in Antarctic micrometeorites. *Meteorit Planet Sci* **40**, 225–238.

Genge M. J. and Grady M. M. (1999) The fusion crusts of stony meteorites: implications for the atmospheric reprocessing of extraterrestrial materials. *Meteorit. Planet. Sci.* **34**, 341–356.

Genge M. J., Grady M. M. and Hutchison R. (1997) The textures and compositions of fine-grained Antarctic micrometeorites: implications for comparisons with meteorites. *Geochim. Cosmochim. Acta* **61**, 5149–5162.

Genge M. J., Suttle M. and Van Ginneken M. (2017) Thermal shock fragmentation of Mg silicates within scoriaceous micrometeorites reveal hydrated asteroidal sources. *Geology* **45**, 891–894.

Goderis S., Soens B., Huber M. S., McKibbin S., Van Ginneken M., Van Maldeghem F., Debaille V., Greenwood R. C., Franchi I. A., Cnudde V. and Van Malderen S. (2020) Cosmic spherules from Widerøefjellet, Sør Rondane Mountains (East Antarctica). *Geochim. Cosmochim. Acta* **270**, 112–143.

Gonczi R., Froeschlé C. and Froeschlé C. (1982) Poynting-Robertson drag and orbital resonance. *Icarus* **51**, 633–654.

Goodrich C. A., Zolensky M. E., Fioretti A. M., Shaddad M. H., Downes H., Hiroi T., Kohl I., Young E. D., Kita N. T., Hamilton V. E. and Riebe M. E. (2019) The first samples from Almahata Sitta showing contacts between ureilitic and chondritic lithologies: implications for the structure and composition of asteroid 2008 TC 3. *Meteorit. Planet. Sci.* **54**, 2769–2813.

Gounelle M., Engrand C., Maurette M., Kurat G., McKeegan K. D. and Brandstatter F. (2005) Small Antarctic micrometeorites: a mineralogical and in situ oxygen isotope study. *Meteorit. Planet. Sci.* **40**, 917–932.

Greenwood R. C., Lee M. R., Hutchison R. and Barber D. J. (1994) Formation and alteration of CAIs in Cold Bokkeveld (CM2). *Geochim. Cosmochim. Acta* **58**, 1913–1935.

Greshake A., Bischoff A. and Hoppe P. (1996) Mineralogy, chemistry, and oxygen isotopes of refractory inclusions from stratospheric interplanetary dust particles and micrometeorites. *Meteorit. Planet. Sci.* **31**, 739–748.

Greshake A., Kloeck W., Arndt P., Maetz M., Flynn G. J., Bajt S. and Bischoff A. (1998) Heating experiments simulating atmospheric entry heating of micrometeorites: Clues to their parent body sources. *Meteorit. Planet. Sci.* **33**, 267–290.

Grossman J. N. and Brearley A. J. (2005) The onset of metamorphism in ordinary and carbonaceous chondrites. *Meteorit. Planet. Sci.* **40**, 87–122.

Hertwig A. T., Defouilloy C. and Kita N. T. (2018) Formation of chondrules in a moderately high dust enriched disk: evidence from oxygen isotopes of chondrules from the Kaba CV3 chondrite. *Geochim. Cosmochim. Acta* **224**, 116–131.

Hervig R. L. and Steele I. M. (1992) Oxygen isotope analysis of Allende olivine by ion probe and implications for chondrule origin. *Lunar Planet. Sci.* **33**, 525–526.

Hiyagon H. and Hashimoto A. (1999) ^{16}O excesses in olivine inclusions in Yamato-86009 and Murchison chondrites and their relation to CAIs. *Science* **283**, 828–831.

Hoppe P., Kurat G., Walter J. and Maurette M. (1995) Trace elements and oxygen isotopes in a CAI-bearing micrometeorite from Antarctica. *Lunar Planet. Sci.* **26**, 623–624.

Imae N., Taylor S. and Iwata N. (2013) Micrometeorite precursors: clues from the mineralogy and petrology of their relict minerals. *Geochim. Cosmochim. Acta* **100**, 113–157.

Ireland T. R., Avila J., Greenwood R. C., Hicks L. J. and Bridges J. C. (2020) Oxygen isotopes and sampling of the Solar System. *Space Sci. Rev.* **216**, 1–60.

Isa J., Kohl I. E., Liu M.-C., Wasson J. T., Young E. D. and McKeegan K. D. (2017) Quantification of oxygen isotope SIMS matrix effects in olivine samples: correlation with sputter rate. *Chem. Geol.* **458**, 14–21.

Itoh S., Kojima H. and Yurimoto H. (2004) Petrography and oxygen isotopic compositions in refractory inclusions from CO chondrites. *Geochim. Cosmochim. Acta* **68**, 183–194.

Ivanova M. A., Lorenz C. A., Franchi I. A., Bychkov A. Y. and Post J. E. (2013) Experimental simulation of oxygen isotopic exchange in olivine and implication for the formation of metamorphosed carbonaceous chondrites. *Meteorit. Planet. Sci.* **48**, 2059–2070.

Ivanova M. A., Lorenz C. A., Nazarov M. A., Brandstaetter F., Franchi I. A., Moroz L. V., Clayton R. N. and Bychkov A. Y. (2010) Dhofar 225 and Dhofar 735: Relationship to CM2 chondrites and metamorphosed carbonaceous chondrites, Belgica-7904 and Yamato-86720. *Meteorit. Planet. Sci.* **45**, 1108–1123.

Jacquet E., Piralla M., Kersaho P. and Marrocchi Y. (2021) Origin of isolated olivine grains in carbonaceous chondrites. *Meteorit. Planet. Sci.* **56**, 13–33.

Jones R. H., Leshin L. A., Guan Y., Sharp Z. D., Durakiewicz T. and Schilk A. J. (2004) Oxygen isotope heterogeneity in chondrules from the Mokoia CV3 carbonaceous chondrite. *Geochim. Cosmochim. Acta* **68**, 3423–3438.

Jones R.H., (1996). Relict grains in chondrules: evidence for chondrule recycling. In: Chondrules and the protoplanetary disk, 163

Joswiak D. J., Nakashima D., Brownlee D. E., Matrajt G., Ushikubo T., Kita N. T., Messenger S. and Ito M. (2014) Terminal particle from Stardust track 130: probable Al-rich chondrule fragment from comet Wild 2. *Geochim. Cosmochim. Acta* **144**, 277–298.

Joy K. H., Tartèse R., Messenger S., Zolensky M. E., Marrocchi Y., Frank D. R. and Kring D. A. (2020) The isotopic composition of volatiles in the unique Bench Crater carbonaceous chondrite impactor found in the Apollo 12 regolith. *Earth Planet. Sci. Lett.* **540** 116265.

Kebukawa Y., Ito M., Zolensky M. E., Greenwood R. C., Rahman Z., Suga H., Nakato A., Chan Q. H., Fries M., Takeichi Y. and Takahashi Y. (2019) A novel organic-rich meteoritic clast from the outer solar system. *Sci. rep.* **9**, 1–8.

Kimura M., Imae N., Komatsu M., Barrat J. A., Greenwood R. C., Yamaguchi A. and Noguchi T. (2020) The most primitive CM chondrites, Asuka 12085, 12169, and 12236, of subtypes 3.0–2.8: their characteristic features and classification. *Polar Sci.* **26** 100565.

King A. J., Bates H. C., Krietsch D., Busemann H., Clay P. L., Schofield P. F. and Russell S. S. (2019) The Yamato-type (CY) carbonaceous chondrite group: analogues for the surface of asteroid Ryugu? *Geochem.* **79** 125531.

Kita N. T., Ushikubo T., Fu B. and Valley J. W. (2009) High precision SIMS oxygen isotope analysis and the effect of sample topography. *Chem. Geol.* **264**, 43–57.

Kita N. T., Nagahara H., Tachibana S., Tomomura S., Spicuzza M. J., Fournelle J. H. and Valley J. W. (2010) High precision SIMS oxygen three isotope study of chondrules in LL3 chondrites: role of ambient gas during chondrule formation. *Geochim. Cosmochim. Acta* **74**, 6610–6635.

Klöck W., Thomas K. L., McKay D. S. and Palme H. (1989) Unusual olivine and pyroxene composition in interplanetary dust and unequilibrated ordinary chondrites. *Nature* **339**, 126–128.

Krot A. N., Amelin Y., Bland P., Ciesla F. J., Connelly J., Davis A. M., Huss G. R., Hutcheon I. D., Makide K., Nagashima K. and Nyquist L. E. (2009) Origin and chronology of chondritic components: a review. *Geochim. Cosmochim. Acta* **73**, 4963–4997.

Krot A. N., Nagashima K., Fintor K. and Pál-Molnár E. (2019) Evidence for oxygen-isotope exchange in refractory inclusions from Kaba (CV3.1) carbonaceous chondrite during fluid-rock interaction on the CV parent asteroid. *Geochim. Cosmochim. Acta* **246**, 419–435.

Krot A. N., Nagashima K., Lyons J. R., Lee J.-E. and Bizzarro M. (2020) Oxygen isotopic heterogeneity in the early solar system inherited from the protosolar molecular cloud. *Sci. Adv.* **6**, eaay2724.

Krot A. N., Yurimoto H., McKeegan K. D., Leshin L., Chaussidon M., Libourel G., Yoshitake M., Huss G. R., Guan Y. and Zanda B. (2006) Oxygen isotopic compositions of chondrules: implications for evolution of oxygen isotopic reservoirs in the inner solar nebula. *Geochem.* **66**, 249–276.

Krot A. N. and Keil K. (2002) Anorthite-rich chondrules in CR and CH carbonaceous chondrites: genetic link between calcium-aluminum-rich inclusions and ferromagnesian chondrules. *Meteorit. Planet. Sci.* **37**, 91–111.

Kurat G., Hoppe P., Walter J., Engrand C. and Maurette M. (1994a) Oxygen isotopes in spinels from Antarctic micrometeorites (abstract). *Meteoritics* **29**, 487–488.

Kurat G., Koeberl C., Presper T., Brandstatter F. and Maurette M. (1994b) Petrology and geochemistry of Antarctic micrometeorites. *Geochim. Cosmochim. Acta* **58**, 3879–3904..

Leshin L. A., Rubin A. E. and McKeegan K. D. (1997) The oxygen isotopic composition of olivine and pyroxene from CI chondrites. *Geochim. Cosmochim. Acta* **61**, 835–845.

Lodders K. (2003) Solar system abundances and condensation temperatures of the elements. *Astrophy. J.* **59**, 1220–1247.

Love S. G. and Brownlee D. E. (1991) Heating and thermal transformation of micrometeoroids entering the Earth's atmosphere. *Icarus* **89**, 26–43.

MacPherson G. J. and Huss G. R. (2005) Petrogenesis of Al-rich chondrules: evidence from bulk compositions and phase equilibria. *Geochim. Cosmochim. Acta* **69**, 3099–3127.

MacPherson G. J., Wark D. A. and Armstrong J. T. (1988) Primitive material surviving in chondrites: refractory inclusions. *Meteorit. Early Solar Syst.*, 746–807.

Makide K., Nagashima K., Krot A. N., Huss G. R., Hutcheon I. D. and Bischoff A. (2009) Oxygen- and magnesium-isotope compositions of calcium–aluminum-rich inclusions from CR2 carbonaceous chondrites. *Geochim. Cosmochim. Acta* **73**, 5018–5050.

Marrocchi Y. and Chaussidon M. (2015) A systematic for oxygen isotopic variation in meteoritic chondrules. *Earth Planet. Sci. Lett.* **430**, 308–315.

Marrocchi Y., Bekaert D. V. and Piani L. (2018a) Origin and abundance of water in carbonaceous asteroids. *Earth Planet. Sci. Lett.* **482**, 23–32.

Marrocchi Y., Villeneuve J., Batanova V., Piani L. and Jacquet E. (2018b) Oxygen isotopic diversity of chondrule precursors and the nebular origin of chondrules. *Earth Planet. Sci. Lett.* **496**, 132–141.

Marrocchi Y., Euverte R., Villeneuve J., Batanova V., Welsch B., Ferrière L. and Jacquet E. (2019) Formation of CV chondrules by recycling of amoeboid olivine aggregate-like precursors. *Geochim. Cosmochim. Acta* **247**, 121–141.

Maruyama S. and Yurimoto H. (2003) Relationship among O, Mg isotopes and the petrography of two spinel-bearing compound chondrules. *Geochim. Cosmochim. Acta* **67**, 3943–3957.

Maruyama S., Yurimoto H. and Sueno S. (1999) Oxygen isotope evidence regarding the formation of spinel-bearing chondrules. *Earth Planet. Sci. Lett.* **169**, 165–171.

Matrajt G., Guan Y., Leshin L., Taylor S., Genge M., Joswiak D. and Brownlee D. (2006) Oxygen isotope measurements of individual unmelted Antarctic micrometeorites. *Geochim. Cosmochim. Acta* **70**, 4007–4018.

Maurette M., Olinger C., Christophe M.-L., Kurat G., Pourchet M., Brandstatter F. and Bourot-Denise M. (1991) A collection of diverse micrometeorites recovered from 100 tonnes of Antarctic blue ice. *Nature* **351**, 44–47.

Miller K. E., Lauretta D. S., Connolly, Jr, H. C., Berger E. L., Nagashima K. and Domanik K. (2017) Formation of unequilibrated R chondrite chondrules and opaque phases. *Geochim. Cosmochim. Acta* **209**, 24–50.

Nagashima K., Krot A. N. and Huss G. R. (2015) Oxygen-isotope compositions of chondrule phenocrysts and matrix grains in Kakangari K-grouplet chondrite: implication to a chondrule-matrix genetic relationship. *Geochim. Cosmochim. Acta* **151**, 49–67.

Nakashima D., Ushikubo T., Joswiak D. J., Brownlee D. E., Matrajt G., Weisberg M. K., Zolensky M. E. and Kita N. T. (2012) Oxygen isotopes in crystalline silicates of comet Wild 2: a comparison of oxygen isotope systematics between Wild 2 particles and chondritic materials. *Earth Planet. Sci. Lett.* **357**, 355–365.

Nesvorný D., Vokrouhlický D., Bottke W. F. and Sykes M. (2006) Physical properties of asteroid dust bands and their sources. *Icarus* **181**, 107–144.

Noguchi T., Ohashi N., Tsujimoto S., Mitsunari T., Bradley J. P., Nakamura T., Toh S., Stephan T., Iwata N. and Imae N. (2015) Cometary dust in Antarctic ice and snow: past and present chondritic porous micrometeorites preserved on the Earth's surface. *Earth Planet. Sci. Lett.* **410**, 1–11.

Plane J. M. C. (2012) Cosmic dust in the earth's atmosphere. *Chem. Soc. Rev.* **41**, 6507–6518.

Prasad M. S., Rudraswami N. G. and Panda D. K. (2013) Micrometeorite flux on earth during the last ~50,000 years. *J. Geophy. Res.* **118**, 2381–2399.

Prasad M. S., Rudraswami N. G., Araujo A. A. and Khedekar D. (2018) Characterisation, sources and flux of unmelted micrometeorites on Earth during the last ~50,000 years. *Sci. Rep.* **8**, 8887.

Rojas J., Duprat J., Engrand C., Dartois E., Delauche L., Godard M., Gounelle M., Carrillo-Sánchez J. D., Pokorný P. and Plane J. M. C. (2021) The micrometeorite flux at Dome C (Antarctica), monitoring the accretion of extraterrestrial dust on Earth. *Earth Planet. Sci. Lett.* **560**, 116794.

Rowe M. W., Clayton R. N. and Mayeda T. K. (1994) Oxygen isotopes in separated components of CI and CM meteorites. *Geochim. Cosmochim. Acta* **58**, 5341–5347.

Rudraswami N. G., Fernandes D. and Pandey M. (2020a) Probing the nature of extraterrestrial dust reaching the Earth's surface collected from the Maitri station, Antarctica. *Meteorit. Planet. Sci.* **55**, 2256–2266.

Rudraswami N. G., Genge M. J., Marrocchi Y., Villeneuve J. and Taylor S. (2020b) The oxygen isotope compositions of large numbers of small cosmic spherules: implications for their sources and the isotopic composition of the upper atmosphere. *J. Geophys. Res. Planet* **125**, e2020JE006414.

Rudraswami N. G., Prasad M. S., Jones R. H. and Nagashima K. (2016a) In situ oxygen isotope compositions in olivines of different types of cosmic spherules: An assessment of relationships to chondritic particles. *Geochim. Cosmochim. Acta* **194**, 1–14.

Rudraswami N. G., Shyam P. M., Dey S., Plane J. M. C., Feng W., Carrillo-Sánchez J. D. and Fernandes D. (2016b) Ablation and Chemical Alteration of Cosmic Dust Particles during Entry into the Earth's Atmosphere. *Astrophy. Supp. Series* **227**.

Rudraswami N. G., Prasad M. S., Nagashima K. and Jones R. H. (2015) Oxygen isotopic composition of relict olivine grains in cosmic spherules: Links to chondrules from carbonaceous chondrites. *Geochim. Cosmochim. Acta* **164**, 57–70.

Rudraswami N. G., Ushikubo T., Nakashima D. and Kita N. T. (2011) Oxygen isotope systematics of chondrules in Allende CV3 chondrite: high precision ion microprobe studies. *Geochim. Cosmochim. Acta* **75**, 7596–7611.

Rudraswami N. G., Marrocchi Y., Shyam P. M., Fernandes D., Villeneuve J. and Taylor S. (2019) Oxygen isotopic and chemical composition of chromites in micrometeorites: Evidence of ordinary chondrite precursors. *Meteorit. Planet. Sci.* **54**, 1347–1361.

Russell S. S., MacPherson G. J., Leshin L. A. and McKeegan K. D. (2000) 16O enrichments in aluminum-rich chondrules from ordinary chondrites. *Earth Planet. Sci. Lett.* **184**, 57–74.

Ruzicka A., Floss C. and Hutson M. (2008) Relict olivine grains, chondrule recycling, and implications for the chemical, thermal, and mechanical processing of nebular materials. *Geochim. Cosmochim. Acta* **72**, 5530–5557.

Schneider J. M., Burkhardt C., Marrocchi Y., Brennecka G. A. and Kleine T. (2020) Early evolution of the solar accretion disk inferred from Cr-Ti-O isotopes in individual chondrules. *Earth Planet. Sci. Lett.* **551**, 116585.

Schrader D. L., Connolly, Jr, H. C., Lauretta D. S., Nagashima K., Huss G. R., Davidson J. and Domanik K. J. (2013) The formation and alteration of the Renazzo-like carbonaceous chondrites II: Linking O-isotope composition and oxidation state of chondrule olivine. *Geochim. Cosmochim. Acta* **101**, 302–327.

Schrader D. L., Davidson J., Greenwood R. C., Franchi I. A. and Gibson J. M. (2014) A water–ice rich minor body from the early Solar System: the CR chondrite parent asteroid. *Earth Planet. Sci. Lett.* **407**, 48–60.

Schrader D. L., Franchi I. A., Connolly, Jr, H. C., Greenwood R. C., Lauretta D. S. and Gibson J. M. (2011) The formation and alteration of the Renazzo-like carbonaceous chondrites I: implications of bulk-oxygen isotopic composition. *Geochim. Cosmochim. Acta* **75**, 308–325.

Scott E. R., Krot A. N. and Sanders I. S. (2018) Isotopic dichotomy among meteorites and its bearing on the protoplanetary disk. *Astrophys. J.* **854**, 164.

Simon J. I., Ross D. K., Nguyen A. N., Simon S. B. and Messenger S. (2019) Molecular cloud origin for oxygen isotopic heterogeneity recorded by a primordial spinel-rich refractory inclusion. *Astrophys. J. Lett.* **884**, L29.

Steele I. M. (1992) Olivine in Antarctic micrometeorites: Comparison with other extraterrestrial olivine. *Geochim. Cosmochim. Acta* **56**, 2923–2929.

Suavet C., Alexandre A., Franchi I. A., Gattacceca J., Sonzogni C., Greenwood R. C., Folco L. and Rochette P. (2010) Identification of the parent bodies of micrometeorites with high-precision oxygen isotope ratios. *Earth Planet. Sci. Lett.* **293**, 313–320.

Suavet C., Cordier C., Rochette P., Folco L., Gattacceca J., Sonzogni C. and Damphoffer D. (2011) Ordinary chondrite related giant (>800 7mm) cosmic spherules from the Transantarctic Mountains, Antarctica. *Geochim. Cosmochim. Acta* **75**, 6200–6210.

Suttle M. D. and Folco L. (2020) The extraterrestrial dust flux: size distribution and mass contribution estimates inferred from the Transantarctic Mountains (TAM) micrometeorite collection. *J. Geophys. Res. Planet.* **125**, e2019JE006241.

Suttle M. D., Dionnet Z., Franchi I., Folco L., Gibson J., Greenwood R. C., Rotundi A., King A. and Russell S. S. (2020) Isotopic and textural analysis of giant unmelted micrometeorites–identification of new material from intensely altered 16O-poor water-rich asteroids. *Earth Planet. Sci. Lett.* **546**, 116444.

Suttle M. D., Genge M. J., Folco L. and Russell S. S. (2017) The thermal decomposition of fine-grained micrometeorites, observations from mid-IR spectroscopy. *Geochim. Cosmochim. Acta* **206**, 112–136.

Suttle M. D., Folco L., Genge M. J., Russell S. S., Najorka J. and Van Ginneken M. (2019) Intense aqueous alteration on C-type asteroids: Perspectives from giant fine-grained micrometeorites. *Geochim. Cosmochim. Acta* **245**, 352–373.

Taylor S., Jones K. W., Herzog G. F. and Hornig C. E. (2011) Tomography: A window on the role of sulfur in the structure of micrometeorites. *Meteorit. Planet. Sci.* **46**, 1498–1509.

Taylor S., Lever J. H. and Harvey R. P. (1998) Accretion rate of cosmic spherules measured at the South Pole. *Nature* **392**, 899–903.

Taylor S., Lever J. H. and Harvey R. P. (2000) Numbers, types and compositions of an unbiased collection of cosmic spherules. *Meteorit. Planet. Sci.* **35**, 651–666.

Taylor S., Matrajt G. and Guan Y. (2012) Fine-grained precursors dominate the micrometeorite flux. *Meteorit. Planet. Sci.* **47**, 550–564.

Taylor S., Matrajt G., Lever J. H., Joswiak D. J. and Brownlee D. E. (2007) Size distribution of Antarctic micrometeorites. *Dust Planet. Syst.* **643**, 145–148.

Tenner T. J., Nakashima D., Ushikubo T., Kita N. T. and Weisberg M. K. (2015) Oxygen isotope ratios of FeO-poor chondrules in CR3 chondrites: influences of dust enrichment and H_2O during chondrule formation. *Geochim. Cosmochim. Acta* **148**, 228–250.

Tenner T. J., Ushikubo T., Kurahashi E., Kita N. T. and Nagahara H. (2013) Oxygen isotope systematics of chondrule phenocrysts from the CO3.0 chondrite Yamato 81020: evidence for two distinct oxygen isotope reservoirs. *Geochim. Cosmochim. Acta* **102**, 226–245.

Tenner T. J., Ushikubo T., Nakashima D., Schrader D. L., Weisberg M. K., Kimura M. and Kita N. (2018) Oxygen isotope characteristics of chondrules from recent studies by secondary ion mass spectrometry. In *Chondrules: Records of the Protoplanetary Disk Processes* (eds. S. S. Russel, H. C. Connolly and A. N. Krot). Cambridge Univ. Press, pp. 196–247.

Thiemens M. H., Jackson T., Zipf E. C., Erdman P. W. and Van Egmond C. (1995) Carbon dioxide and oxygen isotope anomalies in the mesosphere and stratosphere. *Science* **270**, 969–972.

Thrane K., Nagashima K., Krot A. N. and Bizzarro M. (2008) Discovery of a new FUN CAI from a CV carbonaceous chondrite: evidence for multistage thermal processing in the protoplanetary disk. *Astrophys. J. Lett.* **680**, L141–L144.

Tomeoka K. and Buseck P. R. (1985) Indicators of aqueous alteration in CM carbonaceous chondrites: microtextures of a layered mineral containing Fe, S, O and Ni. *Geochim. Cosmochim. Acta* **49**, 2149–2163.

Toppani A., Libourel G., Engrand C. and Maurette M. (2001) Experimental simulation of atmospheric entry of micrometeorites. *Meteorit. Planet. Sci.* **36**, 1377–1396.

Tronche E. J., Hewins R. and MacPherson G. J. (2007) Formation conditions of aluminum-rich chondrules. *Geochim. Cosmochim. Acta* **71**, 3361–3381.

Ushikubo T. and Kimura M. (2021) Oxygen-isotope systematics of chondrules and olivine fragments from Tagish Lake C2 chondrite: Implications of chondrule-forming regions in protoplanetary disk. *Geochim. Cosmochim. Acta* **293**, 328–343.

Ushikubo T., Kimura M., Kita N. T. and Valley J. W. (2012) Primordial oxygen isotope reservoirs of the Solar nebula recorded in chondrules in Acfer 094 carbonaceous chondrites. *Geochim. Cosmochim. Acta* **90**, 242–264.

Van Ginneken M., Folco L., Cordier C. and Rochette P. (2012) Chondritic micrometeorites from the Transantarctic Mountains. *Meteorit. Planet. Sci.* **47**, 228–247.

Van Ginneken M., Gattacceca J., Rochette P., Sonzogni C., Alexandre A., Vidal V. and Genge M. J. (2017) The parent body controls on cosmic spherule texture: evidence from the oxygen isotopic compositions of large micrometeorites. *Geochim. Cosmochim. Acta* **212**, 196–210.

Van Schmus W. R. and Wood J. A. (1967) A chemical-petrologic classification for the chondritic meteorites. *Geochim. Cosmochim. Acta* **31**, 747–765.

Weisberg M. K., Ebel D. S., Connolly, Jr, H. C., Kita N. T. and Ushikubo T. (2011) Petrology and oxygen isotope compositions of chondrules in E3 chondrites. *Geochim. Cosmochim. Acta* **75**, 6556–6569.

Wyatt S. P. and Whipple F. L. (1950) The Poynting-Robertson effect on meteor orbits. *Astrophys. J.* **111**, 134–141.

Yada T., Nakamura T., Noguchi T., Matsumoto N., Kusakabe M., Hiyagon H., Ushikubo T., Sugiura N., Kojima H. and Takaoka N. (2005) Oxygen isotopic and chemical compositions of cosmic spherules collected from the Antarctic ice sheet: implications for their precursor materials. *Geochim. Cosmochim. Acta* **69**, 5789–5804.

Yada T., Nakamura T., Takaoka N., Noguchi T., Terada K., Yano H., Nakazawa T. and Kojima H. (2004) The global accretion rate of extraterrestrial materials in the last glacial period estimated from the abundance of micrometeorites in Antarctic glacier ice. *Earth Planets Space* **56**, 67–79.

Yamanobe M., Nakamura T. and Nakashima D. (2018) Oxygen isotope reservoirs in the outer asteroid belt inferred from oxygen isotope systematics of chondrule olivines and isolated forsterite and olivine grains in Tagish Lake-type carbonaceous chondrites, WIS 91600 and MET 00432. *Polar Sci.* **15**, 29–38.

Young E. D. and Russell S. S. (1998) Oxygen reservoirs in the early solar nebula inferred from an Allende CAI. *Science* **282**, 452–455.

Yu Y., Hewins R. H., Clayton R. C. and Mayeda T. K. (1995) Experimental study of high temperature oxygen isotope exchange during chondrule formation. *Geochim. Cosmochim. Acta* **59**, 2095–2104.

Yurimoto H., Krot A. N., Choi B. G., Aléon J., Kunihiro T. and Brearley A. J. (2008) Oxygen isotopes of chondritic components. *Rev. Mineral. Geochem.* **68**, 141–186.

Zhang M., Bonato E., King A. J., Russell S. S., Tang G. and Lin Y. (2020a) Petrology and oxygen isotopic compositions of calcium-aluminum-rich inclusions in primitive CO3. 0–3.1 chondrites. *Meteorit. Planet. Sci.* **55**, 911–935.

Zhang M., Lin Y., Tang G., Liu Y. and Leya I. (2020b) Origin of Al-rich chondrules in CV chondrites: incorporation of diverse refractory components into the ferromagnesian chondrule-forming region. *Geochim. Cosmochim. Acta* **272**, 198–217.

Zolotov M. Y. (2012) Aqueous fluid composition in CI chondritic materials: chemical equilibrium assessments in closed systems. *Icarus* **220**, 713–729.

Associate editor: Alexander N. Krot